UNIVERSITAT POLITÈCNICA DE CATALUNYA
BARCELONATECH
Escola Superior d'Enginyeries Industrial, Aeroespacial i Audiovisual de Terrassa

Design and Modelling of a Non-linear Spring-mass Energy Harvesting Device for Wind Turbine

Document:
Memòria

Autor/Autora:
Bonet Bach, Jaume

Director/Directora - Codirector/Codirectora:
Garcia-Almiñana, Daniel - Nico, Valeria - Punch, Jeff

Titulació:
Màster en Enginyeria Aeronàutica

Convocatòria:
Primavera, 2022

TREBALL DE FI D'ESTUDIS

Resum

Aquest projecte es centra en el desenvolupament d'un dispositiu de recol · lecció d'energia aplicat a les puntes de pala de turbines de vent. Durant el desenvolupament del treball un dispositiu de recol · lecció d'energia basat en un sistema no linear de massa-molla és triat basant-se en una recerca en l'estat de l'art de dispositius de recol · lecció d'energia a baixes freqüències ($< 10\ Hz$). Un prototip del dispositiu, que es basa en un imant movent-se entre dues molles (amb un volum aproximat de $10x3.5x3.5$ cm^3 i freqüència natural $< 10\ Hz$) és provat per a diferents distàncies entre molles. Addicionalment es desenvolupa un model que té com a objectiu predir la potència generada pel dispositiu. El model consisteix en un sistema electro-dinàmic per representar el comportament dinàmic i elèctric del dispositiu, mitjançant una discretització de la bobina per aproximar l'amortiment magnètic i la forca electromotriu generada. Un anàlisis d'elements finits a través de *COMSOL Multiphysics*, basat en la densitat del camp magnètic romanent, és dut a terme per a determinar el camp magnètic creat per l'imant al centre de la bobina. Els resultats mostren que quan la distancia entre les dues molles s'incrementa de 16 mm a 18 mm, hi ha un canvi en la freqüència natural de 9 Hz a 8 Hz i genera un potencia rms (mitja quadràtica) de 1.53 mW a 1.27 mW respectivament, per una acceleració rms de 0.2 g. Per una acceleració rms de 0.5 g el canvi de freqüència va de 9.5 Hz a 8.5 Hz i la potencia rms va de 2.28 mW a 1.59 mW respectivament. El model és capaç de predir la potència rms generada i el canvi en la freqüència natural per distàncies pròximes a la distància utilitzada per ajustar el model ($+2\ mm$). Una continuació en el desenvolupament del model permetrà mitjançant el codi *MATLAB*, optimitzar les dimensions i principals característiques físiques del dispositiu depenent de les condicions ambientals de les turbines de vent en què hagi de treballar.

Abstract

This project addresses the development of a vibrational energy harvester for deployment at the blade-tips of large-scale wind turbines. In this work, a non-linear single-degree-of-freedom mass-spring system is chosen on the basis of an extensive literature review. An electromagnetic energy harvester based on a magnet moving between two springs (an approximate volume of $10x3.5x3.5$ cm^3 and natural frequency $< 10\ Hz$) is tested experimentally for different distances between the two springs. Additionally, a model that aims to predict the harvester power output is developed. The model consists of a coupled electro-dynamic system to represent the dynamic and the electrical behaviour of the harvester, with the discretization of the coil to approximate the magnetic damping and the electromotive force generated. A finite element analysis carried with *COMSOL Multiphysics*, based on the remanent magnetic field density, is used to determine the magnetic field of the magnet in the centre of the coils. The results show that when the distance between the top and the bottom spring is increased from 16 mm to 18 mm, there is a shift of frequency that goes from 9 Hz to 8 Hz and an rms power generated of 1.53 mW and 1.27 mW, respectively, for a 0.2 g rms acceleration. For a 0.5 g rms acceleration the shift of frequency goes from 9.5 Hz to 8.5 Hz and the rms power generated was 2.28 mW and 1.59 mW respectively. The model is able to predict the power output and the frequency shift for distances between springs close to the one used to tune the model ($+2\ mm$). Further development on the model will allow to use the *MATLAB* scripts to optimise the harvester and obtain its main characteristics for a given wind turbine blade and operational characteristics.

Keywords: Energy Harvesting, Vibrations, Spring-Mass, Electro-Dynamic, Wind Turbines.

Contents

List of Tables

List of Figures

Nomenclature

A	Area (m^2)
B_r	Radial component of the magnetic field (T)
c_e	Electromagnetic damping (N/V)
c_{es}	Electromagnetic damping of the sub-coil (N/V)
c_{mf}	Friction damping (Ns/m)
emf	Electromotive force (V)
emf_s	Electromotive force of the sub-coil (V)
g	Acceleration due to gravity (m/s^2)
g_0	Gap between springs (m)
h_m	Magnet height (m)
h_s	Spring height (m)
I	Intensity (A)
k	Elastic constant (N/m)
l	Length of the sub-coil wire (m)
L_c	Coil inductance (H)
m	Mass of the magnet (kg)
$\hat{n}$	Normal vector to a surface $(-)$
P	Power (W)
r	Runge–Kutta parameter $(-)$
R_c	Coil resistance (Ω)
R_{cs}	Sub-coil resistance (Ω)
R_L	Load resistance (Ω)
t	Time (s)
u	Runge–Kutta variables matrix $(m, m/s, V)$
V_L	Voltage at the load resistance (V)
$\dot{V}_L$	V_L derivative over time (V/s)
$\ddot{y}$	Input acceleration (m/s^2)
z	Position of the lower side of the magnet (m)
$\dot{z}, v$	Velocity of the magnet (m/s)
$\ddot{z}$	Acceleration of the magnet (m/s^2)
γ	Damping coefficient $(-)$
θ	Angular position $(^\circ)$
$\dot{\theta}$	Angular velocity $(^\circ/s)$
$\ddot{\theta}$	Angular acceleration $(^\circ/s^2)$
ϕ_m	Magnetic flux (Wb)

1 INTRODUCTION

1.1 Aim

The field of energy harvesting has arisen over the last two decades due to an increase in the demand for renewable and self-sufficient energy supplies. Energy harvesting technology is a term usually used to refer to small-scale devices (of order of cm or smaller) that can convert ambient energy into electrical energy to power electronic devices. In this project, energy harvesting will be applied to small sensors used in large-scale wind turbines.

One of the key requirements for more efficient wind turbines is the possibility to tilt the angle of attack of the wind turbine blades depending on the incoming wind at the tips. This can be done by placing sensors on the wind turbine tips. The main problem is the power supply, as batteries need to be replaced too often, and direct power feed from the wind turbine centre is not viable. One of the solutions is to power the telemetry by means of an energy harvesting device, which is self-sufficient and has low maintenance [18], which is the objective of this project, and it is explained in the next paragraphs.

The objectives of this project are described in the following lines. The main focus of this project is to understand the state of the art energy harvesting devices for low frequency external vibrations ($< 10\ Hz$), and choose the most suitable approach to create a device capable of powering telemetry that addresses pitch angle monitoring control for large-scale wind turbine installations. A model that can predict the power output of the device for different working conditions is to be developed. Moreover, a *MATLAB* code to be able to run an analysis using the model has to be written. A functional prototype has to be designed and built, and suitable experiments carried out in order to characterise the harvester and validate the model. Finally, a comparison between the simulations and the experiments has to be done to find what are the next steps to improve the model. To do so, the working conditions on wind turbines, a reference telemetry, and a reference blade are required to define the constraints of the project.

1.2 Scope

- Research on the typical environmental conditions the device will have to work on.
- Literature review with conclusion about best methodology to go forward with the project.
- Development of the electro-dynamic model.
- *MATLAB* scripts coding.
- Design and construction of the prototype harvester.
- Test the device for different frequencies, accelerations and load resistances.

- Tune the model with the experimental data.
- Perform and analysis of how well the model simulation predicts the power output and how it can be improved.

1.3 Justification

With global warming, there is an urgency to finish the transition from fossil to renewable energies. To achieve that, the actual technologies need to be improved and become more efficient. In the case of wind turbines, their production can be increased by controlling the tilt angle of the blades depending on the atmospheric conditions. To obtain data of the incoming wind at the wind turbine tips, like its velocity or its direction, a group of sensors need to be placed in the blades. To feed this telemetry, a direct connection with the ground is discarded as it would require a lot of cable and the installation would require a lot of manpower. Batteries are left aside too as their lifespan is too short, and access to the interiors of wind turbines is very difficult and costly. One of the best ways to feed the telemetry would be through an energy harvesting device that is self-sufficient and that has a long lifespan. This project will set the foundations to develop an energy harvesting device capable of generating enough power to feed telemetry for different wind turbine tips.

2 MOTION TO ELECTRICITY CONVERSION

2.1 Physics of Electromagnetic Generators

In this section, the physics behind the conversion of the movement of a coil in a magnetic field (or the movement of a magnetic field in a coil) into electricity will be covered. That electricity can later be stored as energy in a battery or can be used directly to feed some sensor or machine.

The following theory is from [2], and all units will be in SI if other ones are not specified.

The magnetic flux that goes through a surface, is the integral of the magnetic field $\vec{B}$ multiplied by the vector normal to the surface $\hat{n}$ over the surface and the area dA. The drawing can be found on Figure 2.1.

$$\phi_m = \int^S \vec{B} \cdot \hat{n}\, dA \tag{2.1}$$

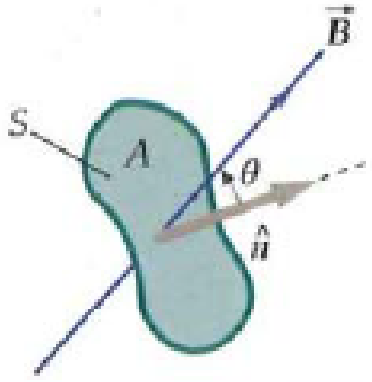

Figure 2.1: *Magnetic flux through a surface [2].*

For a coil with N turns all with the same area, the magnetic flux is simplified to:

$$\phi_m = NBA\cos\theta \tag{2.2}$$

Where θ is the angle between $\vec{B}$ and $\hat{n}$.

The Faraday law of induction says that when the magnetic flux on an electric circuit varies over time, an electromotive force is induced to the circuit. For a circuit with a fixed resistance, the intensity through the circuit can be found. The equations below describes this phenomenon and in figure 2.2 a drawing can be found.

$$emf = -\frac{d\phi_m}{dt} = IR_c \tag{2.3}$$

$$P = emfI = emf^2/R_c \tag{2.4}$$

The - sign is because the induced electromotive force creates a magnetic field that generates a magnetic flux that opposes the initial variation of the magnetic flux.

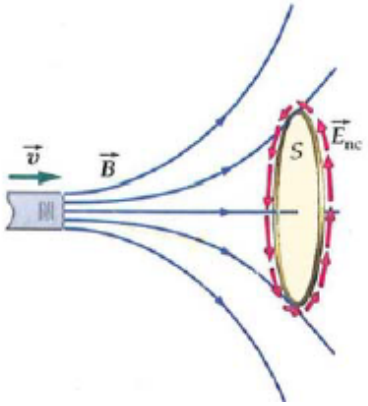

Figure 2.2: *Electromotive force induced by a current variation [2].*

For example for the coil of Figure 2.3, a spire rotating at an angular velocity $\dot{\theta}$ the induced emf is:

$$emf = \dot{\theta}BA\sin\dot{\theta}t \tag{2.5}$$

For N number of turns of the Coil, all with the same area, the emf has to be multiplied by N.

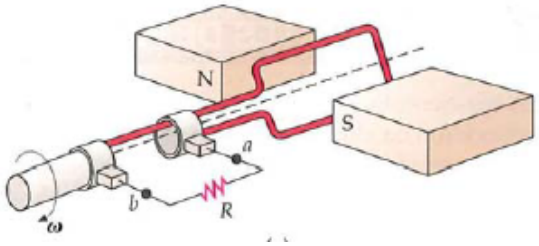

Figure 2.3: *Coil rotating in the middle of the magnetic field created by two magnets [2].*

In a similar way, if a magnet is vibrating inside a coil (note that the magnets do not create an infinite homogeneous magnetic field but one as in Figure 2.4) the magnetic flux will be varying and a current that can be used to feed a battery or a sensor will be induced.

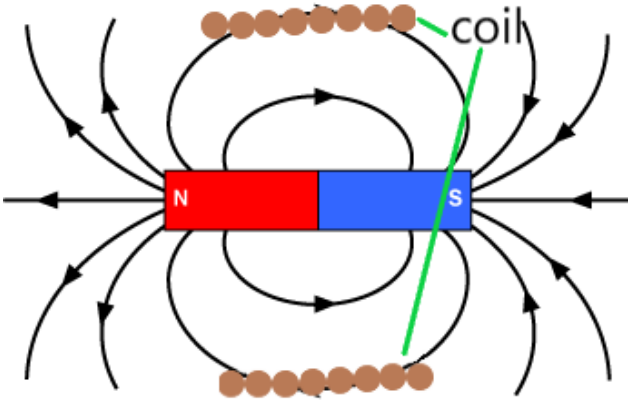

Figure 2.4: *Magnetic field (black arrows) created by a magnet.*

2.2 Piezoelectric Materials

In this section, the equations that govern the transformation of deformation in piezoelectric materials into electric field will be given. From this electric field, energy can be extracted, as in the electromagnetic generators, and stored in batteries or be used directly to feed a sensor.

The following theory to obtain the piezoelectric equations is all extracted from Fang and Liu [1].

The basic piezoelectric equations are:

$$\begin{aligned} \sigma_{ij} &= {c^E}_{ijkl}\varepsilon_{kl} - e_{kij}E_k \\ D_i &= e_{ikl}\varepsilon_{kl} + {k^\varepsilon}_{ik}E_k \end{aligned} \tag{2.6}$$

where σ is the stress tensor, ε is the strain tensor, E is the electric field vector, D is the electric displacement vector and c, e and k are the elastic stiffness, piezoelectric stress and dielectric constants respectively. If the above equations are written in tensor form, we obtain:

$$\begin{aligned} \sigma &= c^E \varepsilon + e^T E \\ E &= e\varepsilon + k^\varepsilon E \end{aligned} \tag{2.7}$$

For the other independent variables we have the following pairs of equations (Fang and Liu [1] extracts this from Laun *et al.* [19]):

$$\begin{aligned} \sigma &= c^D \varepsilon + h^T E D \\ E &= -h\varepsilon + \beta^\varepsilon D \end{aligned} \tag{2.8}$$

$$\begin{aligned} \varepsilon &= S^E \sigma + d^T E \\ D &= d\sigma + k^\varepsilon E \end{aligned} \tag{2.9}$$

$$\begin{aligned} \varepsilon &= S^D \sigma + g^T D \\ E &= -g\sigma + \beta^\sigma E \end{aligned} \tag{2.10}$$

where h, β, S, d, g are the piezoelectric stiffness, dielectric isolation rate, elastic compliance, piezoelectric strain and piezoelectric voltage constants respectively. The superscript D means constant electric displacement, the superscript σ constant stress, and the superscript T means the transpose of the tensor. Which set of equations use will depend on the independent variables of the problem.

In the piezoelectric field is common to change the sub indexes ij and kl for p and q respectively as shown in Table 2.1 .

ij or kl	p or q
11	1
22	2
33	3
23 or 32	4
13 or 31	5
12 or 21	6

Table 2.1: *Change of sub indexes ij and kl for p and q [1]*

Doing that and because of the symmetry of all the tensors used, the matrix form of the tensors can be simplified as seen in Figure 2.5. Tensors s and c, β and k, h and g, d and e have the same dimensions respectively. Here the theory from Fang and Liu [1] ends.

$$\boldsymbol{\sigma} = \begin{bmatrix} \sigma_1(\sigma_{11}) \\ \sigma_2(\sigma_{22}) \\ \sigma_3(\sigma_{33}) \\ \sigma_4(\sigma_{32}) \\ \sigma_5(\sigma_{31}) \\ \sigma_6(\sigma_{12}) \end{bmatrix}, \boldsymbol{\varepsilon} = \begin{bmatrix} \varepsilon_1(\varepsilon_{11}) \\ \varepsilon_2(\varepsilon_{22}) \\ \varepsilon_3(\varepsilon_{33}) \\ \varepsilon_4(2\varepsilon_{32}) \\ \varepsilon_5(2\varepsilon_{31}) \\ \varepsilon_6(2\varepsilon_{12}) \end{bmatrix}, \boldsymbol{c} = \begin{bmatrix} c_{11} & c_{12} & c_{13} & c_{14} & c_{15} & c_{16} \\ c_{12} & c_{22} & c_{23} & c_{24} & c_{25} & c_{26} \\ c_{13} & c_{23} & c_{33} & c_{34} & c_{35} & c_{36} \\ c_{14} & c_{24} & c_{34} & c_{44} & c_{45} & c_{46} \\ c_{15} & c_{25} & c_{35} & c_{45} & c_{55} & c_{56} \\ c_{16} & c_{26} & c_{36} & c_{46} & c_{56} & c_{66} \end{bmatrix}, \boldsymbol{e} = \begin{bmatrix} e_{11} & e_{21} & e_{31} \\ e_{12} & e_{22} & e_{32} \\ e_{13} & e_{23} & e_{33} \\ e_{14} & e_{24} & e_{34} \\ e_{15} & e_{25} & e_{35} \\ e_{16} & e_{26} & e_{36} \end{bmatrix}^T$$

$$\boldsymbol{D} = \begin{bmatrix} D_1 \\ D_2 \\ D_3 \end{bmatrix}, \boldsymbol{E} = \begin{bmatrix} E_1 \\ E_2 \\ E_3 \end{bmatrix}, \boldsymbol{\kappa} = \begin{bmatrix} \kappa_{11} & \kappa_{12} & \kappa_{13} \\ \kappa_{12} & \kappa_{22} & \kappa_{23} \\ \kappa_{13} & \kappa_{23} & \kappa_{33} \end{bmatrix}$$

Figure 2.5: *Examples of how the tensors look after the change of sub indexes [1].*

In Wang [20] and Wedlock [21] can be found that the relationship between D and σ when there is no external magnetic field ($E = 0$) is:

$$\begin{bmatrix} D1 \\ D2 \\ D3 \end{bmatrix} = \begin{bmatrix} 0 & 0 & 0 & 0 & d_{15} & 0 \\ 0 & 0 & 0 & d_{15} & 0 & 0 \\ d_{31} & d_{31} & d_{33} & 0 & 0 & 0 \end{bmatrix} \begin{bmatrix} \sigma_1 \\ \sigma_2 \\ \sigma_3 \\ \sigma_4 \\ \sigma_5 \\ \sigma_6 \end{bmatrix} \tag{2.11}$$

For a beam where there are no shear stresses, which will be most of the cases for the energy harvesting applications, there is only D3. In piezoelectric materials, directions 1,2,3 are associated with the x,y,z directions, and directions 4,5,6 to shear directions y-z, z-x,x-y respectively. If there is a cuboid beam with dimensions L>W>H, then direction 1 is along L dimension, direction 2 is along W dimension, and direction 3 is along H direction.

In [2] we find that the voltage difference between two surfaces with a constant electric field is:

$$V = EH = \frac{QH}{\varepsilon_r \varepsilon_0 A} \tag{2.12}$$

where V is the voltage between two surfaces, E the electric field between the two surfaces, the H is the distance between the two surfaces, A is the area of one of the surfaces, ε_r and ε_0 are respectively the relative permittivity and the vacuum permittivity, and Q is the free charge in each face of the surface. When a piezoelectric beam is deformed, between the upper and the lower surfaces of the beam normal to the direction of the deformation, a constant electric field appears, so we can use the equation above for piezoelectric materials.

Since the integral over a surface of the electric displacement gives us the free charge on that surface [20], if D is constant over the surface, the voltage on the piezoelectric can be now related to the electric displacement as:

$$V = \frac{DH}{\varepsilon_r \varepsilon_0} \tag{2.13}$$

So the typical set of equations for piezoelectric beams used in the energy harvesting applications are:

$$\begin{aligned} D_3 &= d_{3q}\sigma_q \\ V &= \frac{D_3 H}{\varepsilon_r \varepsilon_0} \end{aligned} \tag{2.14}$$

The values of sigma will vary depending on the type of excitation the beam is receiving (vibrations, circular motion, changes of pressure, etc.).

[22] claims that the most used types of piezoelectric materials are PZT (lead zirconate titanate) and PVDF (polyvinylidene fluoride), and there are three ways to excite them: by compression, slap, and bending. From the same paper, the two most common ways to employ piezoelectric materials are explained. The first one is to excite mode 31, by applying a force in direction 1. The other one is to excite mode 33, by applying a force in direction 3. The resulting voltages are:

$$\begin{aligned} V_3 &= \frac{d_{31}F_1}{\varepsilon_r \varepsilon_0 W} = \frac{d_{31}\sigma_1 H}{\varepsilon_r \varepsilon_0} (Mode31) \\ V_3 &= \frac{d_{33}F_3 H}{\varepsilon_r \varepsilon_0 W L} = \frac{d_{33}\sigma_3 H}{\varepsilon_r \varepsilon_0} (Mode33) \end{aligned} \tag{2.15}$$

Those match with the equations 2.14. Which mode will generate more energy, for the same force applied, will depend on the geometry of the piezoelectric, as usually d_{33} is larger than d_{31}, but mode 31 also depends on the ratio L/H. This is if we are comparing the effect of applying a force. If we are comparing the effect of applying a stress, then for the same stress, the mode 33 will generate more energy [22].

For a cantilever beam deflected in the direction of the thin dimension, the internal stresses of deflecting the beam are in direction 1, so mode 13 is excited.

3 ENERGY HARVESTING METHODS: STATE OF THE ART

In this chapter, the main works in the field of energy harvesting aiming to feed wireless sensors are reviewed. Even though there is a wide range of energy harvesting methods, this project will focus on harvesting energy from vibrations or circular motion. Those are believed to be the main source of environmental energy on blade tips. In the two following sections, the most relevant works based on those sources of energy will be reviewed. They will be separated into two types of energy harvesting devices, the ones using electromagnetism and the ones using piezoelectric materials.

In the last section of this chapter, a summary of the salient characteristics of the relevant state-of-the-art harvesters is presented and they will be compared in order to choose the best method to harvest energy for this project.

To have an idea of the characteristics needed from the energy harvester, the conditions on the blade tips are described here.

Research on the wind turbine working conditions was carried to find the general conditions under what the harvester has to produce power, which are:

- Work on low frequencies ($3 - 10\ Hz$ [23], [24], [25]).
- Have a wide bandwidth ($2 - 5\ Hz$).
- Work far from the centre of rotation ($57 - 164\ m$ [26])
- Work on low angular velocities ($5 - 20\ rpm$ are the typical angular velocities of wind turbine blades [26])
- Have a low volume ($< 500\ cm^3$ [27]).

A reference blade and telemetry were chosen in order to define more specific targets and thus be able to constrain the variables of the harvester so that it produces the target power at the target frequency. The target power is extracted from Fischer (2020) [28], and it has a value of $5.5\ mW$. The study made by Broen & Jesper (2003) [29] over a $19.1\ m$ fiberglass and epoxy blade showed that the flap first natural frequency is $2.5\ Hz$ and that the edge first natural frequency is $4.8\ Hz$. The target frequency is then set to $4.8\ Hz$ as it is the highest of the two frequencies and thus more energy can be extracted from it. The next section presents a summary of the literature review of potentially suitable energy harvesters and the final constraints and targets of the project.

3.1 Circular Motion Energy Harvesting

Circular motion energy harvesting consists in obtaining energy from the circular movement of an object. Some examples of how the energy can be harvested are: deformations due to gravity (e.g. a cantilever beam whose deformation changes with the relative position of gravity like in Ramirez *et al.* (2019)[10]), change in the momentum (e.g. a car wheel when it accelerates or breaks like in Lee *et al.* (2012)[3]) or the deformation due to contact forces (e.g. a part of a tire when it touches the floor like in Bowen and Arafa (2015) [30]).

In the following subsections, different experiments testing circular motion energy harvester devices will be explained. Papers and articles whose designs can not be adapted to the tips of a wind turbine blade will be discarded. For example, designs using deformations due to contact forces as the blade deformations at small scales are small. Devices working at high frequencies, which are not found in the wind turbines, are left out of the study too. Finally, devices that work for high rotational speed are discarded because, as stated before, the rotational speed of wind turbines is very small.

3.1.1 State of the Art: Electromagnetic Generators

In this section, some of the main works on circular motion energy harvesting methods using electromagnetic generators will be summarised.

An innovative energy harvester device is found in Lee *et al.* (2012)[3]. Instead of using the constant circular motion of an object, it uses changes in momentum. The design consists of an iron arm connected to a DC motor through a gearbox. At the tip of the arm, there is an off-axis mass and at the base of the support, a magnet is placed to hold the arm down and increase the velocity at which the arm starts rotating. A Schematic of the device is shown in Figure 3.1.

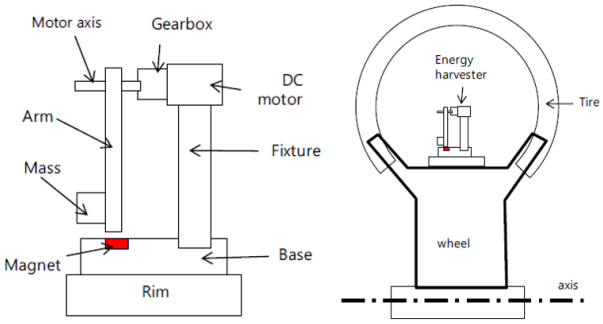

Figure 3.1: *Schematic of the energy harvester design [3].*

The working principle is that below a certain rotational speed the magnetic force is bigger than

the centrifugal force. Once the critical rotational speed is surpassed, the centrifugal force is bigger than the magnetic force and the arm starts to rotate. In the beginning, it rotates slowly but once it has separated a small distance from the magnet, the magnetic force drops, and then the arm rotates very fast to the outside of the wheel. When the speed drops enough so the magnetic force is higher than the centrifugal force again, it comes back to the initial position due to gravity and stays there. This happens every rotation when the part of the wheel where the device is placed touches the floor because the centrifugal force there is 0 (the movement during the contact with the floor is lineal). The working procedure is represented in Figure 3.2. Even though the arm only rotates 180°, each half-rotation generates multiple rotations on the DC generator. This is due to the gearbox between the arm and the DC generator. The key aspect of energy generation is how fast the arm rotates. The higher the magnetic force is, the faster it will rotate when it reaches the critical velocity.

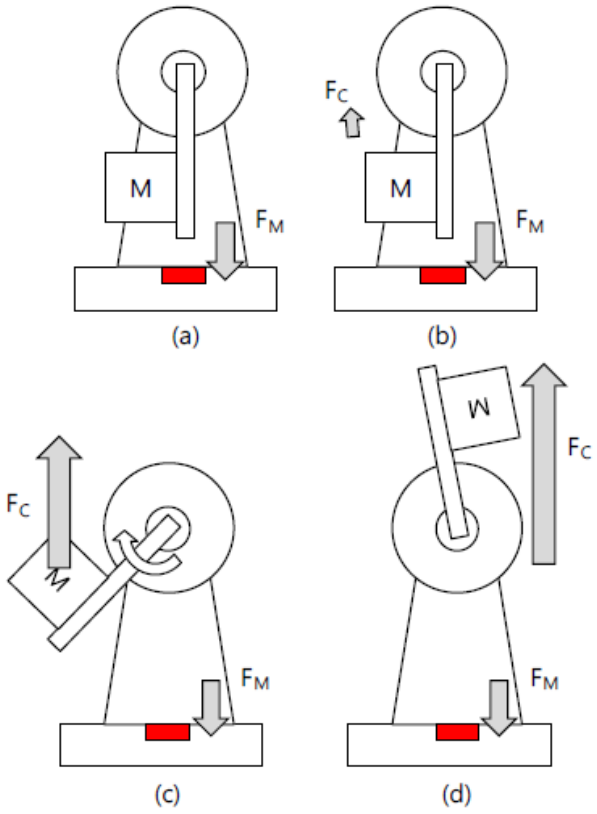

Figure 3.2: *Working principle of the energy harvester [3].*

The experimental results done with this device prove that even the device is producing energy during 10% of the experiment time, the energy produced during the short time period is enough to feed small wireless sensors. It must be remarked that the paper does not perform any kind of optimization, meaning the device have a large margin of improvement. A power peak of 56 mW was achieved for a 3 Hz frequency. The paper does not provide information on the device at different rotational speeds.

Another novel rotational energy harvester device, using gravitational torque, is proposed in Toh *et al.* (2007)[4]. The device works similarly to an electromagnetic generator. It has a stator attached to any point of the rotating structure, and then a rotor with an off-centered mass. A magnetic torque is created, that will make the rotor spin together with the stator, and here is where the off-center mass plays an essential role. The off-center mass generates a torque that opposes the magnetic one. A diagram of the torques acting on the device is shown in Figure 3.3.

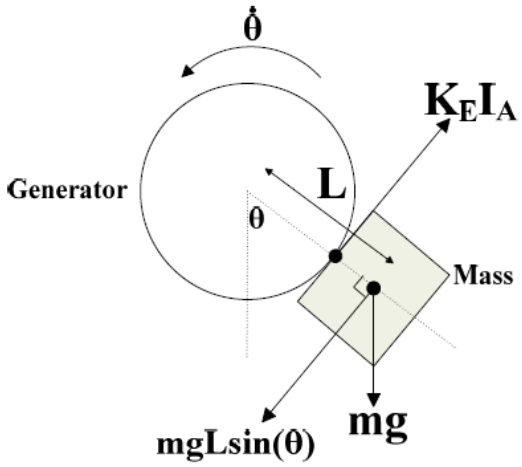

Figure 3.3: *Diagram of the torques acting on the energy harvester device [4].*

The maximum power that can be extracted is $P = mgL\dot{\theta}$ because mgL is the maximum torque that the gravitational force can generate. The experiment done shows that an average power from $10mW$ can be extracted for a frequency range of $10Hz$. Additionally, a study on the effect of placing the generator out of the axis of rotation was done. The motion of the off-axis harvester is like the one of a double pendulum ($\ddot{\theta}_2 = [r_1\dot{\theta}_1^2 \sin\theta_1 - \theta_2 - g\sin\theta_2]/r_2$), see Figure 3.4. The centrifugal force pulls the mass outwards, making the rate of change $\theta_1 - \theta_2$ smaller. Toh *et al.* solved the double pendulum equation for different off-axis distances and rotational speeds and observed that the power generated decreased substantially and became chaotic if normal accelerations are greater than 1 g.

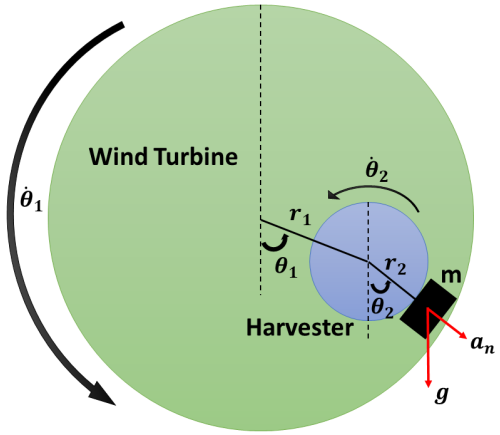

Figure 3.4: *Schematic of a harvester based on the circular motion placed off-axis.*

3.1.2 State of the Art: Piezoelectric Materials

In this section, some of the main papers on circular motion energy harvesting methods using piezoelectrics will be summarised.

Febbo *et al.* (2016)[5] proposes an energy harvester system that consisted of 2 aluminum beams connected with a mass. One of these two beams has a PZT (lead zirconate titanate, which is a piezoelectric material) beam attached to it so when the aluminium beam is deformed, the deformation is carried to the piezoelectric beam. The mass of the two-beam system is attached to a spring that has a larger mass at the other end, supported with 4 aluminium beams. All this is on a rigid frame, mounted at some distance of the axis of rotation. A scheme is shown in Figure 3.5.

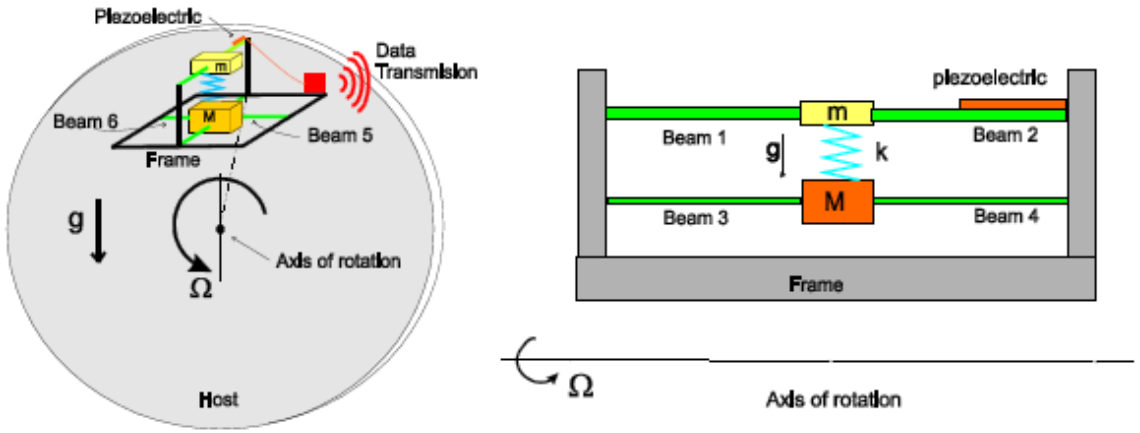

Figure 3.5: *Schematic of the energy harvester [5].*

Two more configurations are proposed and studied in the paper. One configuration consists of only one beam attached to each mass, and the other one consists of only two beams attached to each mass. After performing some experiments, the results show that for low rotational speeds the best configuration is the two-beam configuration. This configuration also shows self-tuning (this is the phenomenon where the natural frequency of the structure changes to match the excitation frequency autonomously) for a rotational speed range between $4.0 - 4.5\ Hz$. The maximum generation frequencies predicted and the experimental ones do not match, which means the model used is only useful to get an order of magnitude but not to obtain exact values. The maximum power output is $1.14\ mW$ for $4.35\ Hz$ and has a bandwidth of $0.1\ Hz$.

A design of a self-turning energy harvester for rotation applications at low frequencies is found in Gu and Livermore (2011)[6]. It consists of a relatively rigid beam made of a piezoelectric material, and a more flexible circular driving beam with a mass attached to its tip. Both beams act like cantilever beams. The device has to rotate in the vertical plane in order for the gravity to act on tip mass. A schematic is shown in Figure 3.6.

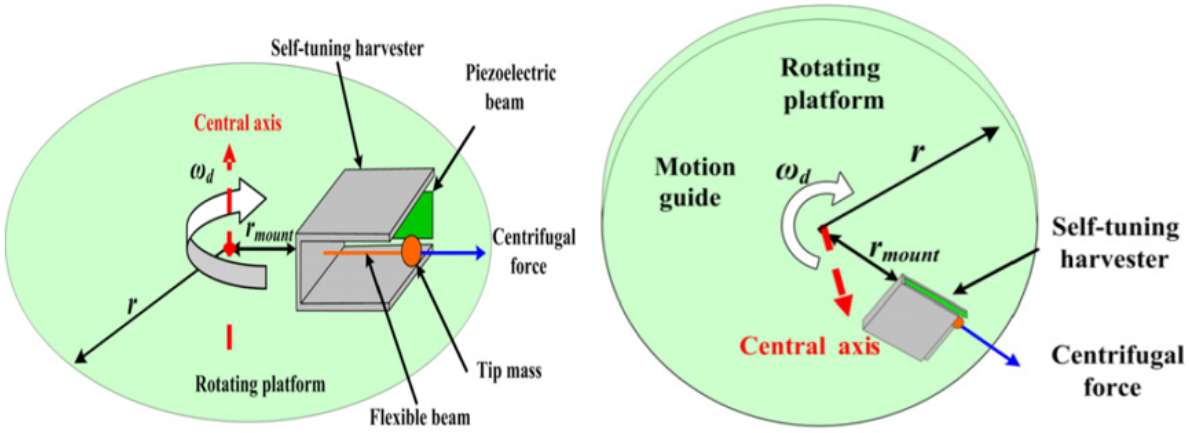

Figure 3.6: *Schematic of the self-tuning energy harvester [6].*

Before performing the experiments, the dimensions of the beams and the mass are optimised to obtain a self-tuning effect over a wide frequency range. Two experiments are done with a PZT (lead zirconate titanate) beam and a PVDF (polyvinylidene fluoride) beam, both piezoelectric materials. The results obtained, validated the analytical model used to optimize the energy harvester, and showed a successful behaviour of the self-tuning technology. It produces a power of $83\ \mu W$ for $10\ Hz$ and has a bandwidth of $4.0\ Hz$.

Another interesting approach to energy harvester devices is the one designed by Mei *et al.* (2019)[7], which consists of an asymmetric tri-stable energy harvester (ATEH). It consists of a cantilever beam with two piezoelectric patches attached to it and a magnet on the tip. Two fixed magnets are set at a certain distance from the magnet at the tip of the beam. A schematic is shown in Figure 3.7.

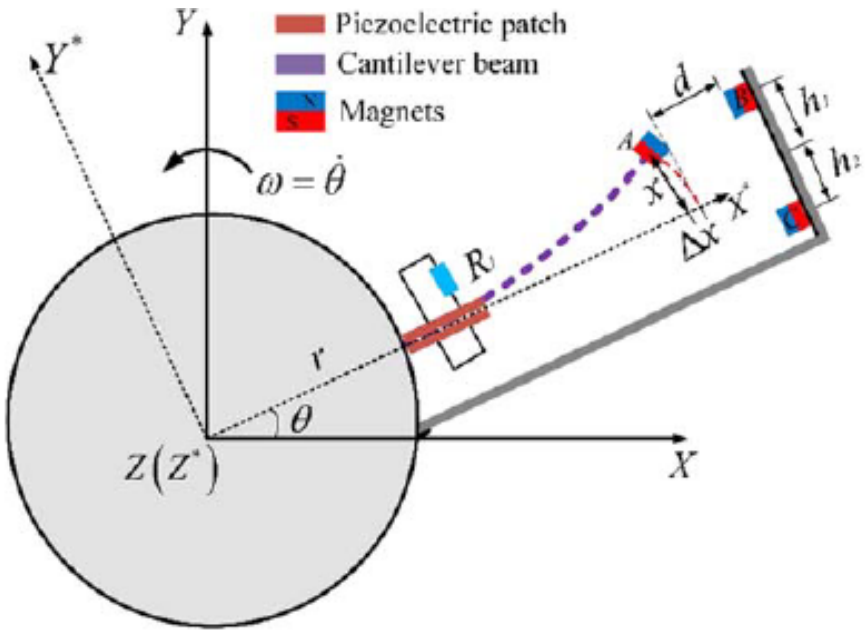

Figure 3.7: *Schematic of the asymmetric tri-stable energy harvester [7].*

The purpose of the paper is to predict the behaviour of the ATEH and compare it to a symmetric TEH (STEH). A mathematical model shows that the ATEH will be excited for lower frequencies than the STEH, as well as for the same frequencies. What the asymmetry provokes is to have an extra inter-well oscillation at a lower frequency than the main one, and means the object oscillates between two potential wells. This inter-well oscillation is when the most energy is created.

The experimental results on the paper validate the model and get to two main conclusions. The first one is that the maximum output power of the ATEH is higher than the one produced by the STEH. The second one is that the low-frequency inter-well oscillations produce a considerable amount of power. This power is smaller than the one produced by the higher frequency inter-well oscillations. This means that the ATEH has a broader frequency range at which it harvests energy than the STEH. A peak power of 0.5 mW is obtained for 6.0 Hz. Its bandwidth is approximately 0.33 Hz. Even if the bandwidth is narrow, the frequency range for which the harvester produces a significant power is 5.4 Hz

A promising method for low rotating frequencies is proposed in Fu and Yeatman (2017)[8]. It consists of a rotating disk with one magnet attached, and a static part with a cantilever beam with a piezoelectric material attached, and a magnet in its tip. A Schematic is in Figure 3.8.

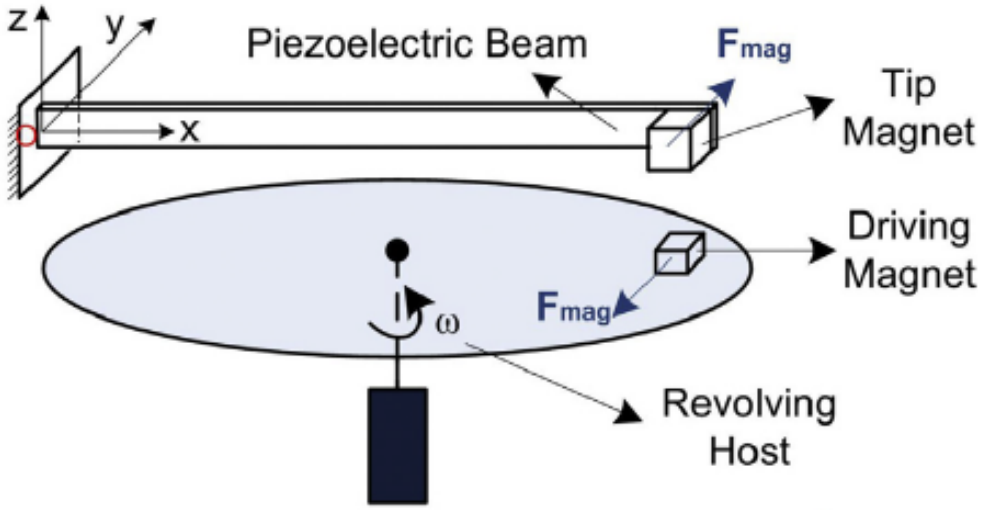

Figure 3.8: *Schematic of the energy harvester [8].*

The device is based on the fact that when the magnet on the disk gets closer to the magnet on the beam, they will repel or attract each other, causing the beam to deflect. Once the magnet on the rotating disk passes the beam, the beam will start to vibrate at its natural frequency, with an exponential decay, and thus the piezoelectric on the beam will produce electricity. This creates a frequency up-conversion each rotation, making the device suitable for a broadband of low-frequencies.

Diverse configurations were studied, but the best one for low frequencies was with the two magnets repelling each other in the direction normal to the rotation plane. The experiments also showed that more than 20 μW were generated for the frequency range of $15 - 35$ Hz, but for less than 10 Hz the power would drop under 10 μW.

A similar design was published by Wu *et al.* (2018)[9] a year later. The design is conceptually the same as in Fu and Yeatman (2017)[8], but in this case, the magnets attract each other and there are two rotating magnets separated 180°. A Schematic is on Figure 3.9.

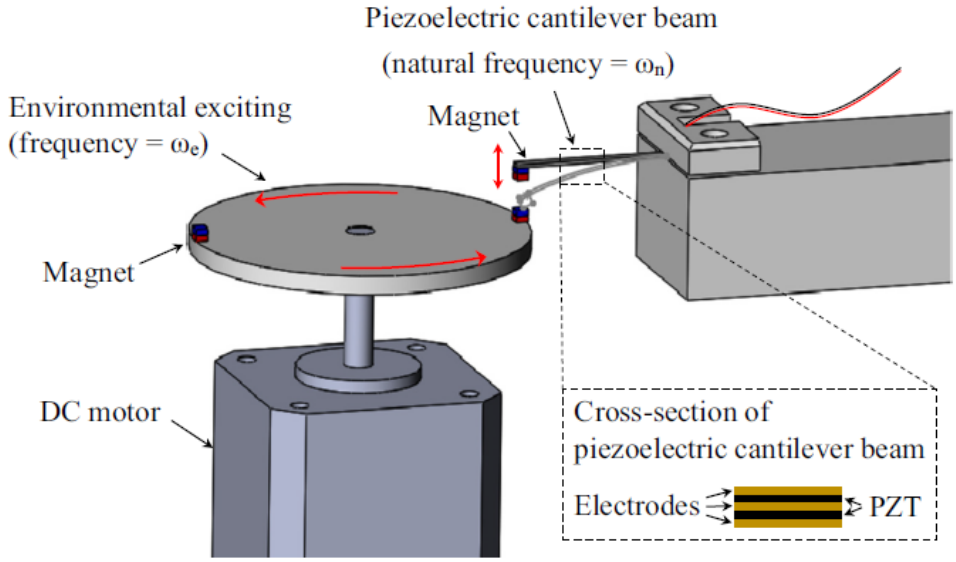

Figure 3.9: *Schematic of the energy harvester [9].*

In this design, the working principle is the same as the one previously shown. Each time the magnet passes by the beam, it produces a magnetic force and excites the beam. If there is only one magnet, the frequency of the external force is the rotating frequency. If more magnets are added, the magnetic force frequency increase. For example, if there are two magnets speared by 180°, the magnetic force frequency is double of the rotating frequency because for each rotation the beam is excited twice. By doing this, low-frequency rotations can be used to produce higher frequency excitations.

Three designs were tested. The first one is just one magnet with attractive force. The second design was two magnets, which were tested with 2 repulsive forces, 2 attractive forces, 1 attractive, and 1 repulsive. For this second design, the most effective was the attractive repulsive forces. The third design was 4 magnets alternating repulsive and attractive forces. The results showed that the 4 magnet configuration was a much better design, doubling the amount charged on a capacitor after 35 seconds compared to the second design, and it is also 10 times better than the first design. For a frequency of 9.4 Hz a power of 0.76 mW was generated. The frequency bandwidth is 2.5 Hz.

A novel design is proposed in Ramirez *et al.* (2019)[10], a multi-beam energy harvester for frequencies less than 3 Hz named MBT2ML. The energy harvester is made of two E shape aluminum beams linked by a rigid steel beam. The lower beams have steel masses at their tips. A schematic is on Figure 3.10.

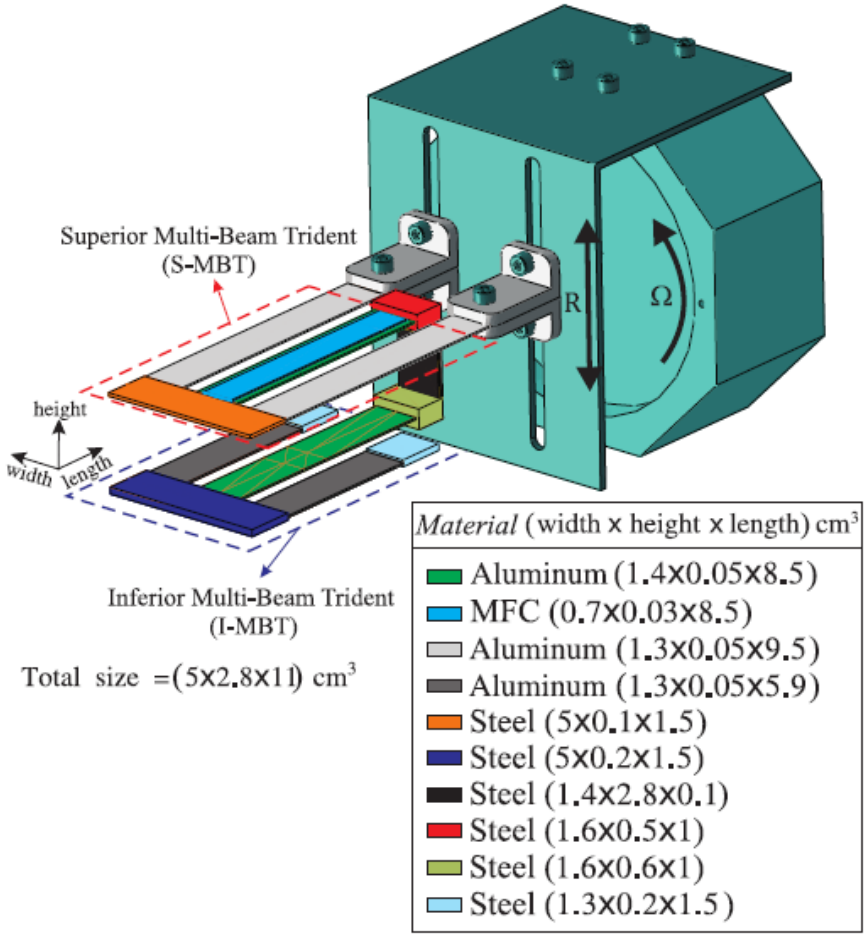

Figure 3.10: *Schematic of the energy harvester [10].*

The piezoelectric sheet can be placed at any of the top beams. For the tests, 3 configurations will be tested, a central unimorph placement, a lateral unimorph placement and a central bimorph placement. A Finite Element (FE) formulation is developed to predict the dynamic behaviour and the power generated for the energy harvester. Experiments with the 3 configurations are performed and the results show that the FE formulation gives a good approach, and using it, it is found that the best configuration is the central unimorph placement. The MBT2ML generates a maximum electric power of 700 μW for 3 Hz (180 rpm) when it is placed at 0.03 m of the rotating axis.

3.2 Vibration Energy Harvesting

In this section, a review of the main works focused on energy harvesting devices will be done. Vibrations are one of the main sources of environmental energy, and one of the most popular topics on small-scale energy harvesting [22]. Low-frequency vibrations are present on the wind turbines blade tips so these types of devices can be used there to harvest energy.

3.2.1 State of the Art: Electromagnetic Generators

In this section, some of the main works on vibration energy harvesting methods using electromagnetic generators will be summarised.

A novice energy harvester design is proposed in Haroun *et al.* (2015)[11], in which a magnet moves freely inside of a coil and impacts against springs. The main difference between a conventional electromagnetic energy harvester (CEEH) and the free impact electromagnetic energy harvester (FIEEH) is that the magnet inside the coil has a distance of free movement before impacting on one of the ends of the frame. Two springs are placed at the end of the frame or attached to each side of the magnet in order to create an oscillatory movement on the magnet inside the frame. A coil surrounds the frame and the movement of the magnet inside it produces a variable magnetic flux, and thus an emf on the coil. A schematic is shown in Figure 3.11.

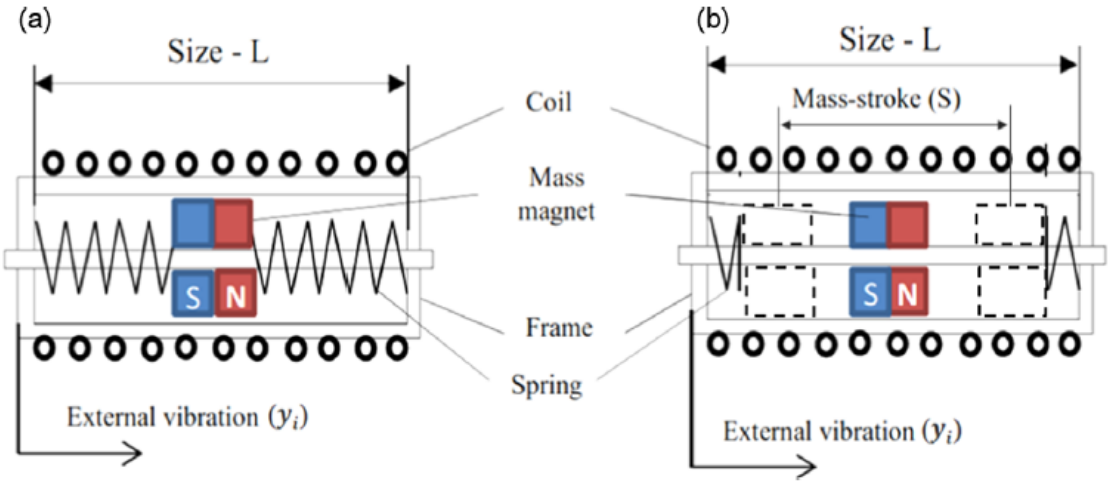

Figure 3.11: *In (a) the schematic of a conventional electromagnetic energy harvester and in (b) the schematic of the energy harvester [11].*

The purpose of the paper is to compare a CEEH with a FIEEH. Both a simulation and an experiment are carried with a CEEH and a FIEEH, both tuned at the same frequency. The results show that for this frequency the FIEEH gives 12 times more power than the CEEH. Additionally, the

experiment shows that the FIEEH with an excitation of 10 Hz and an amplitude of 0.0 $1m$ can generate 0.35 W. The bandwidth of the device is approximately 2 Hz.

In Halim *et al.* (2018)[12] an EH using a sprung eccentric rotor has been designed. It consists of a fixed circular disc with ten connected coils, and two iron discs at each side, and each one has a rotor with ten magnets (in a N-S-N-S-... series). This lateral discs have an eccentric mass, covering half of the disc perimeter, and are attached to a torsional spring. A scheme is shown in Figure 3.12.

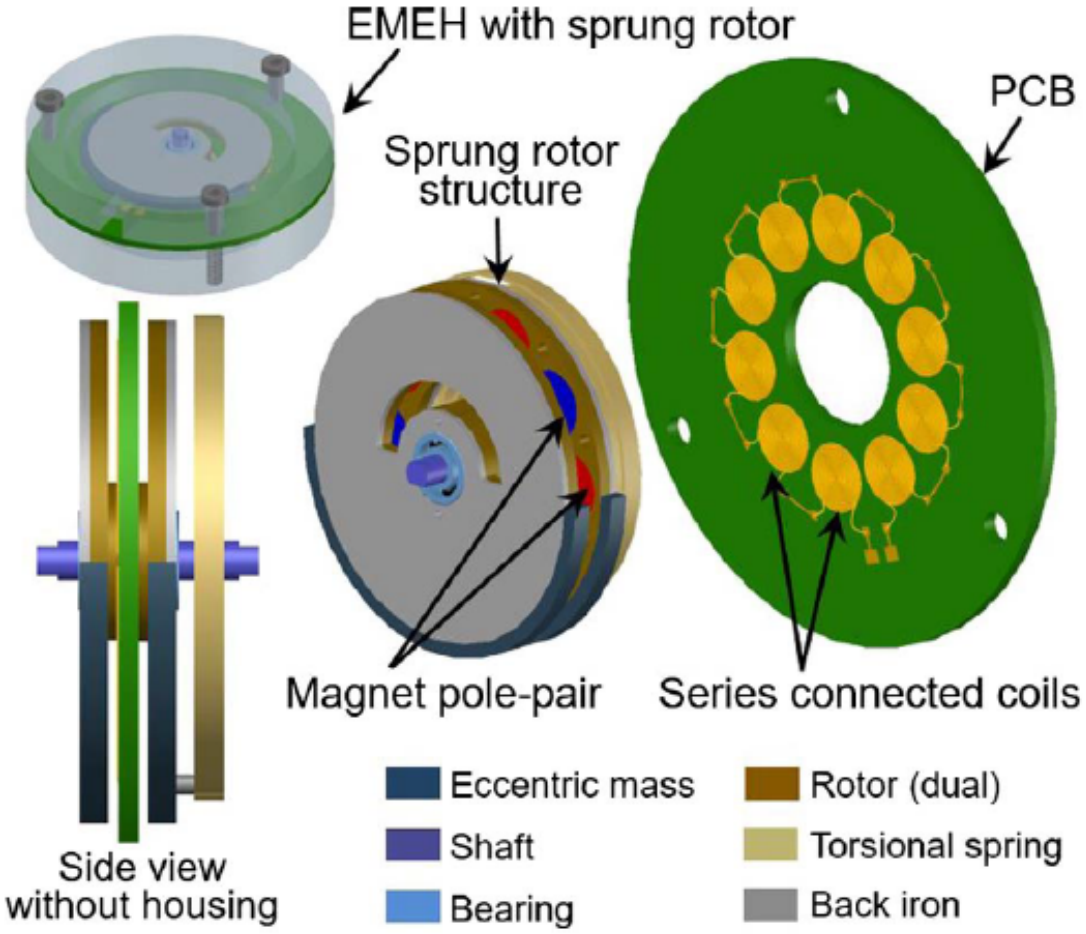

Figure 3.12: *Scheme of the 2 degree-of-freedom energy harvester [12].*.

This device works with circular vibrations. The eccentric mass moves due to linear accelerations

of the motion and also due to gravity, rotating the side disks. The spring creates a torque that opposes the movement. The stiffness of the spring is a key parameter to optimise the device to a certain frequency. The experimental results show that for a well desired device, the power obtained for a frequency of 1.25 Hz is 60 μW for a swing motion of $\pm 12.5°$. It has a bandwidth of 0.2 Hz.

An energy harvester with frequency up-conversion is proposed in Ashraf *et al.* (2013)[13] which has a good broadband of working frequencies. The design has 3 parts that can be seen in Figure 3.13. The first one is a pickup coil attached to an acrylic platform employing an elastic beam to create a high-frequency resonator. Then, four magnets with steel keepers are attached to the platform to create a magnetic closed circuit. Finally, the whole setup is attached to a case using two flexible beams to form a low-frequency resonator.

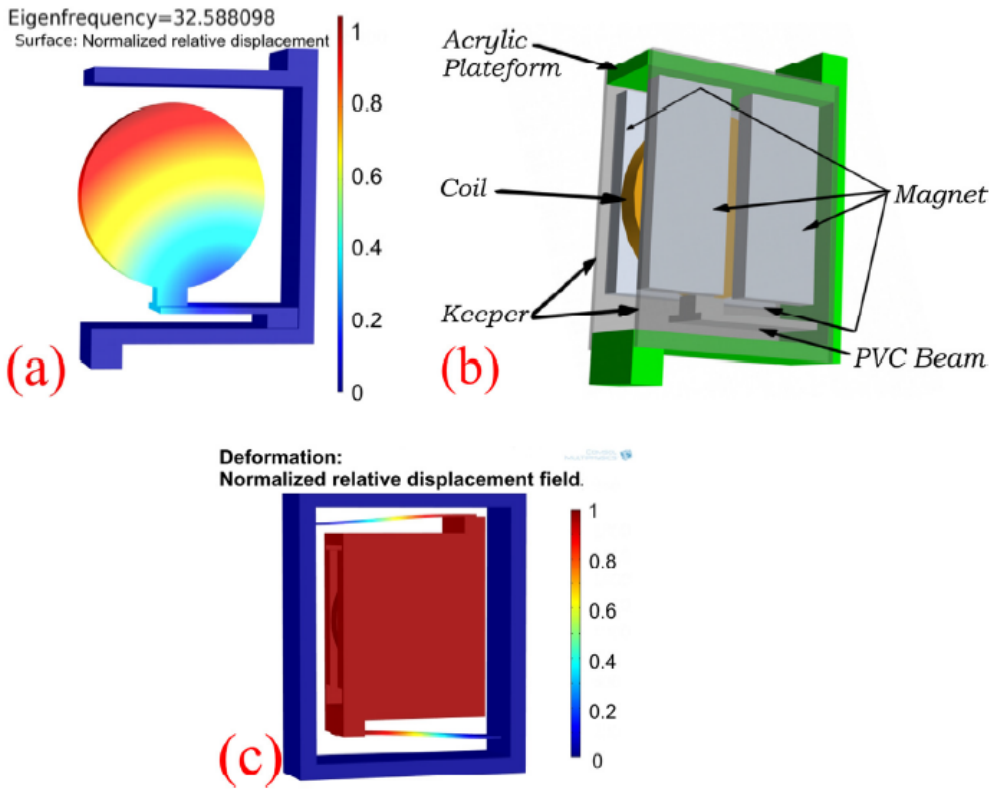

Figure 3.13: *In (a) the inner structure with the coil, in (b) the setup of the magnets and the coil and in (c) the inner resonator together with the outer resonator [13].*

The theory behind this device is that when the amplitude of oscillation of the low-frequency resonator is big enough, it impacts against the case, transferring its energy to the high-frequency

oscillator, and this one will oscillate freely until the next impact. The analytical model and the experiments show that the frequency resonator has 5 different power peaks in the range of $0-18\ Hz$. For the test, the prototype of the energy harvester was exited at 10.3 Hz, producing a useful power of 26 μW for an acceleration of 0. $5m/s^2$ and a power of 5.02 mW for an acceleration of 9.8 m/s^2. The bandwidth of the device is approximately 2.5 Hz. The authors claim that to their knowledge, this device is the one that has a higher power density for low frequencies.

A novice design of a 2 degree-of-freedom energy harvester is presented at Valeria *et al.* (2016)[14]. The device consists of a primary mass that has a set of seven coils that oscillate vertically between two magnets that act as a spring-mass. Inside this coil, there is a secondary mass made up of five stacked magnets that oscillates vertically between two other magnets that act as a magnetic spring. A schematic is shown in Figure 3.14.

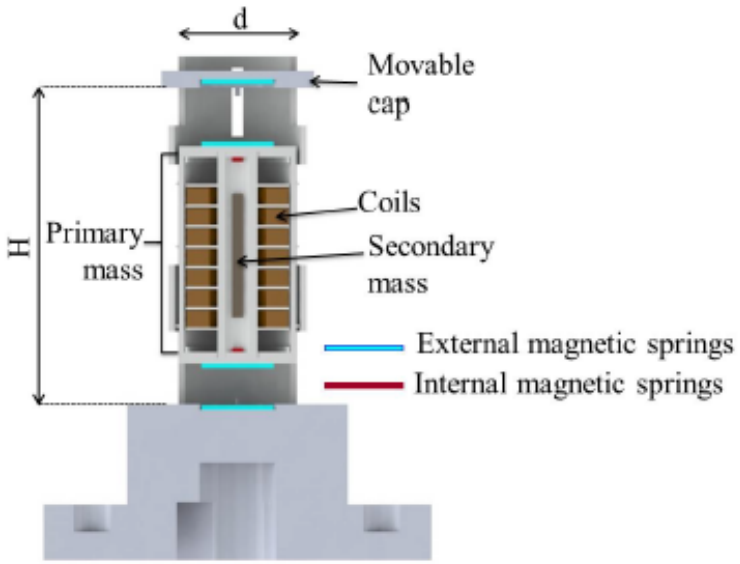

Figure 3.14: *Schematic of the 2 degree-of-freedom energy harvester [14].*

The working principle of the device is that the energy from the movement of the primary mass is transferred to the secondary mass. Because of the primary mass being heavier than the secondary mass, the vibration of the secondary mass is higher than the primary one, enabling the device to extract energy from low-frequency vibrations in a more efficient way. The experimental results of the paper show that for a frequency of 11.5 Hz the maximum power produced is 2.06 mW with an acceleration of 3.9 m/s^2. The bandwidth is approximately 4 Hz.

3.2.2 State of the Art: Piezoelectric Materials

In this section, some of the main papers on vibration energy harvesting methods using piezoelectric will be summarised.

A basic piezoelectric energy harvester for low frequencies is studied in Zhao *et al.* (2018)[31]. This study will be useful as a base to compare to other more complex designs and decide if the increase in complexity is worth the increase in the power harvested. The design is a simple piezoelectric bimorph cantilever beam with a mass on its tip. Depending on the frequency of the excitation, the beam will deflect more or less, and thus harvest more or less power.

The experiments performed in two models of 140mm and 160mm length, produced a power of 1.04 mW at 8.79 Hz and 1.97 mW at 8.83 Hz respectively. It is a good amount of power. The problem with this simple design is that it has a very narrow bandwidth, in this case of only 0.5 Hz.

Wang *et al.* (2017)[15] suggests another energy harvester in which frequency up-conversion is proposed. The special characteristic of this impact-based energy harvester is that it has a quintuple-well potential. The device consists of a cantilever metallic driving beam with a magnet on its tip, which acts as a proof mass. At a certain distance on each side, there are 4 other metallic beams with piezoelectric material on them, which have a smaller Young's modulus than the driving beam. Two fixed magnets are placed under the magnet on the driving beam at a certain distance, one at each side of it, in a way an attractive force appears. A schematic is shown in Figure 3.15.

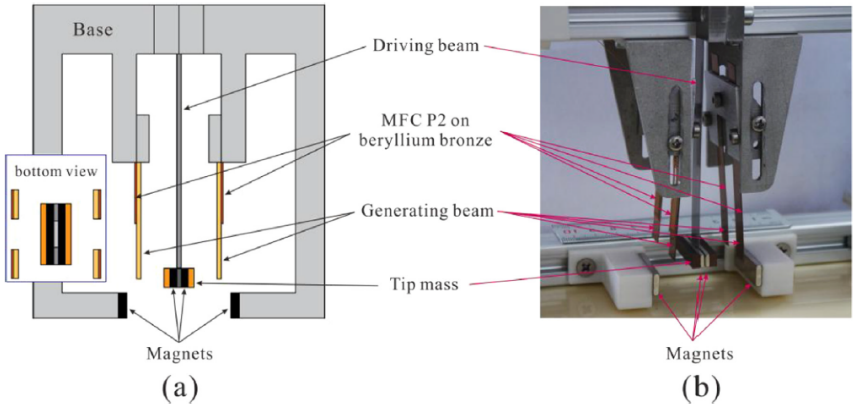

Figure 3.15: *In (a) a schematic of the device and in (b) an image of the fabricated prototype [15].*

When a frequency close to the natural frequency of the driving beam and a large enough excitation act on the energy harvester, the driving beam starts vibrating, impacting the generating beams periodically. During a short time, the driving and the generating beams vibrate together, but when they separate, the generating beam vibrates at its own natural frequency (higher than the one of the driving beam) until the next impact.

The experiments performed on the prototype reveal that the quintuple-well potential energy harvester can produce up to 35 times more power over a wider frequency range than its convectional counterpart (which does not have the fixed magnets). The prototype produced a 7.25 mW at 10 Hz for an acceleration of 7 m/s^2. It has a bandwidth of 4 Hz for 7 m/s^2.

In Liu and Livermore (2015)[16] a design of an energy harvester that passively switches among dynamical modes, with a large operational range is presented. The device consists of a driving beam with U shape and a tip mass at the end. A piezoelectric cantilever beam that acts as a generating beam is placed inside the driving beam. Both beams are mounted in the same support, and the driving beam has a flexible tip that is in contact with the generating beam. A schematic is shown in Figure 3.16.

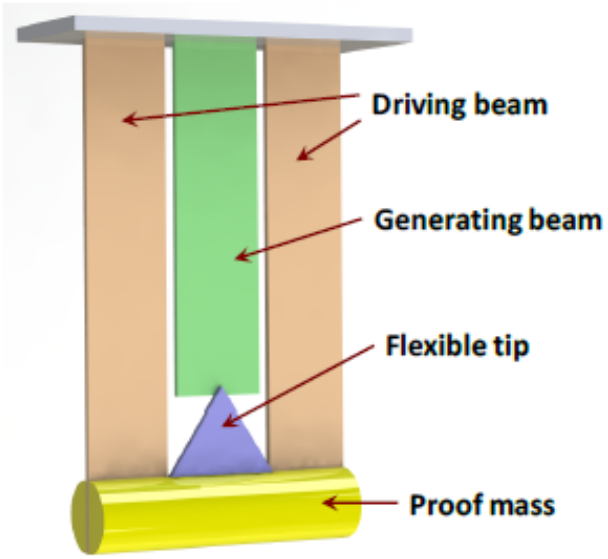

Figure 3.16: *Schematic of piezoelectric energy harvester with stoppers [16].*

For small accelerations, the driving beam and the generating beam move together for half an oscillation and during the other half, the generating beam can oscillate freely. For larger or on resonance accelerations, the driving beam deflects the generating beam until the flexible tip is plucked, leading

to a period of free oscillation for the generating beam.

The results of the experiments done with this harvester display that for a stiffer tip, a power peak of 0.267 mW for an acceleration of 14.7 m/s^2 at a frequency of 7 Hz. Fore a flexible tip the power peak is 0.036 mW for an acceleration of 14.7 m/s^2 at a frequency of 7 Hz, but the plucked harvesting mode appears for a wider frequency range, which is the one that produces more power. This means that depending on the levels of acceleration of the vibrations on the environment a more stiff or a more flexible tip will be more appropriate. The frequency bandwidth is around 2 Hz.

A piezoelectric energy harvester with stoppers is proposed in Fan *et al.* (2019)[17] to try to overcome the issues with low levels of excitation. The design is quite simple, and it consists of bimorph cantilever beam with two magnets attached at the tip of it, one at each side. Symmetrically at each side of the beam tip, there is a stopper followed by a fixed magnet. A schematic is shown in Figure 3.17.

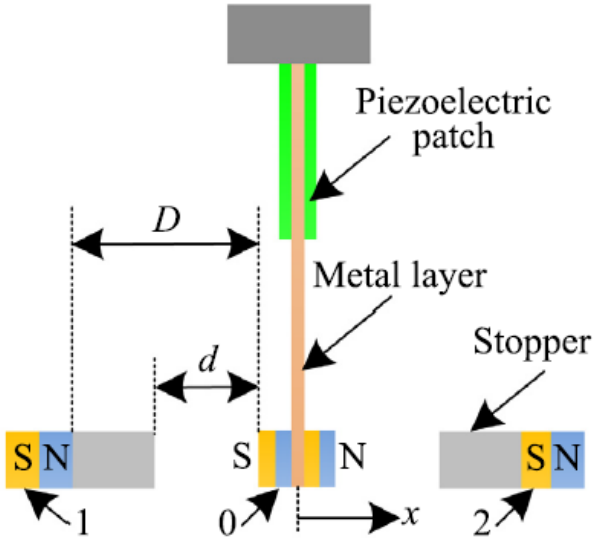

Figure 3.17: *Schematic of piezoelectric energy harvester with stoppers [17].*

The working principle of the energy harvester is that the attraction magnetic force produced when the cantilever beam is out of its equilibrium position increase the deflections of the beam, making the device able to produce useful power from low-level excitations. The experiments performed show that for low frequencies it can create a power of 0.055 mW for an acceleration of 1.5 m/s^2. The frequency bandwidth is approximately 2.5 Hz.

3.3 Summary and Comparison

All the energy harvesting methods reviewed have been tested to find the frequencies at which they can produce more energy, but have not been tested under specific work conditions. The objective of the project is to design a device that can extract enough energy to feed a sensor in a reliable way, on the wind turbine blade tips. In this section, the different devices reviewed will be compared to find the best approach to achieve the objective of this project. In table 3.1 a summary of the main characteristics of the reviewed devices can be found.

Author	Type	Input		Device	Electric
		Frequency (Hz)	Bandwidth (Hz)	Main dimension (mm)	power (mW)
[3]	Circular	3.0	-	50	56.0
[4]	Circular	3.0	2.5	150	2.00
[5]	Circular	4.35	0.1	200	1.14
[6]	Circular	10.0	4.0	20	0.083
[7]	Circular	6.0	0.33	115	0.50
[8]	Circular	10.0	4.0	27	0.01
[9]	Circular	9.4	2.5	35	0.76
[10]	Circular	3.0	-	110	0.70
[11]	Vibration	10.0	2.0	100	350
[12]	Vibration	1.25	0.2	40	0.06
[13]	Vibration	10.3	2.5	35	5.02
[14]	Vibration	11.5	-	57	2.06
[31]	Vibration	8.83	0.5	160	1.97
[15]	Vibration	10.0	4.0	105	0.725
[16]	Vibration	7.0	2.0	36	0.267
[17]	Vibration	9.0	2.5	63	0.055

Table 3.1: *Table with the main characteristics of the different devices reviewed.*

The device proposed by Lee *et al.* (2012)[3] is discarded because the acceleration and deceleration process on the wind turbines are very slow and this would create very few situations in which the device would activate. The works from Mei *et al.* (2019)[7], Fu and Yeatman (2017)[8], Wu *et al.* [9], Ramirez *et al.* (2019)[10] or Toh *et al.* (2007)[4] require two parts of the harvester to have a relative circular motion. This can only be achieved in a natural way by either placing one part in the fixed in the wind turbine stator and one in the rotor (which is discarded because the harvester must be at the blade tips) or by having an off-axis mass. The latest option does not work in the case of wind turbines because at blade tips the centrifugal force is between 1.6 (5 rpm and 57 m) and 73 (20 rpm and 164 m) times larger than the gravitational force, as the power generated decreased substantially [4]. Finally, the methods described in Febbo *et al.* (2016)[5] and in Gu and Livermore

(2011)[6], which consists of deforming a piezoelectric beam using the change of direction of gravity, have not been studied for large centrifugal accelerations, so they are also discarded.

Regarding the vibration energy harvesters, Halim *et al.* (2018)[12] is discarded due to the low amplitude of the circular vibrations at the blade tips. The fact that we are working with random aerodynamic vibrations, implies that devices with a broad bandwidth are the best suited to the task, making them capable of harvesting on a wider range of vibrations. This leaves us with Haroun *et al.* (2015)[11], Nico *et al.* (2016)[14], Liu and Livermore (2015)[16] and Fan *et al.* (2019)[17]. From these, Liu and Livermore (2015), and Fan *et al.* (2019) are under $1mW$ of power produced so they are discarded too. Nico *et al.* (2016) performs better for low volume applications, but the results on Haroun *et al.* (2015) show that it can produce up to 350 mW for a device 10 cm long.

After comparing all the devices, the best option to create a functional energy harvester to use in wind turbine tips seems to be the one proposed in Haroun *et al.* (2015)[11]. This is due to the high power output, its simplicity, and a relatively good bandwidth. This will be the starting point to achieve the objective of this research, which is to create a model that can be used to optimise an energy harvesting device for different wind turbines and working conditions.

4 PROPOSED METHOD

In this section, the harvester concept is explained, and then a coupled electro-dynamic model is developed. Then the *MATLAB* code used to obtain the predicted values is explained in detail. In chapter 6 the results of the simulation are presented together with the ones from the experiments.

4.1 Concept

The harvester consists of a magnet that moves between two springs as it can be seen in Figure 4.1. All this is inside a case with copper coils wound around with a 0.15 mm diameter wire. The coils should be as long as the magnet (15 mm), because longer coils would reduce the change in the magnetic flux and, thus, the power generated. The space between the two springs can be varied and needs to be tuned so the harvester has its resonance peak at the desired frequency. The coils are placed in a series anti-series (meaning the wire of the first coil turns clockwise and then the wire of the next coil anti-clockwise, and so on) format because it was experimentally proved that it was the configuration giving the highest power compared to all in series or all in anti-series.

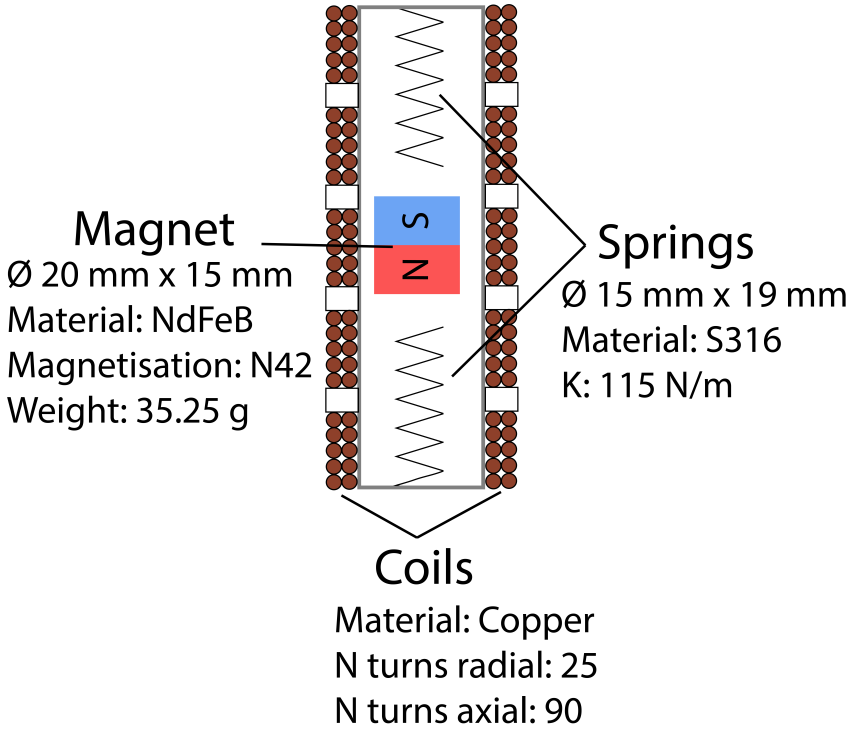

Figure 4.1: *Section of the harvester concept for the project where in this picture axial refers to the vertical direction and radial to the horizontal direction.*

4.1.1 Coupled Electro-Dynamic Model

A coupled electro-dynamic model of the harvester is developed in this subsection in order to predict its output power and frequency response. The magnet is modelled as a mass which creates a magnetic field, that oscillates between two springs and that is affected by mechanical and electro-magnetic damping (c_{mf} and c_e) as seen in Figure 4.2. A very important parameter is the distance between the top and the bottom spring, g_0, which is the main parameter that can be changed in order to shift the natural frequency of the harvester once all the other parameters like the spring constant, the magnet and the coils are constrained.

The model has the following simplifications: gravity can go only in the direction of movement (in reality gravity could change its direction as the blade rotates depending on the directions of the exploited mode); no extra friction coefficient is added when the magnet touches the springs; the coil inductance is calculated using the Wheeler formula [32]; and the electro-magnetic damping is approximated to $\frac{B \cdot L}{R_L} V_L$, where B is the magnetic field, L is the coil length, R_L is the load resistance and V_L is the voltage at the load resistance.

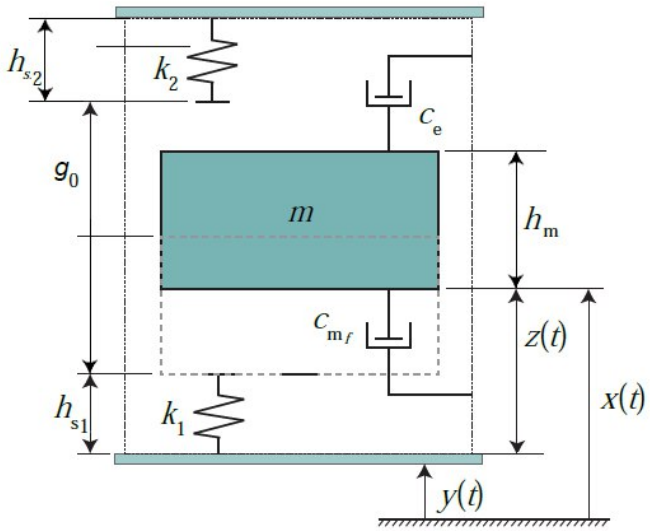

Figure 4.2: *Schematic of the physical model used to predict the harvester behaviour.*

To create the mathematical model, three differential equations are used, one for the velocity, one for the acceleration and one for the derivative of the voltage. The equation for the velocity is used because if only the acceleration and voltage derivative equations were used, the acceleration differential equation would be of second order. By adding the velocity differential equation, three first order differential equations are obtained, which are shown next:

$$\dot{z} = v \tag{4.16}$$

$$\dot{v} = (-kz - c_{mf}\dot{z} - c_e\dot{z} - mg - m\ddot{y})/m \tag{4.17}$$

$$\dot{V_L} = \frac{emfR_L}{L_c\dot{z}}\dot{z} - \frac{R_L + R_c}{L_c}V_L \tag{4.18}$$

where z is the position of the lower side of the magnet, kz is the elastic force of the springs, emf is the electromagnetic force, R_L is the load resistance, R_c is the coil resistance, L_c is the inductance of the coil, m is the mass of the magnet, $\ddot{y}$ is the external input acceleration, c_{mf} is the friction damping, c_e is the electromagnetic damping and V_L is the voltage at the load resistance. With reference to Figure 4.2, the kz term varies with the position as seen in Equation 4.19:

$$kz = \begin{cases} k_1(h_{s1} - z) & z < h_{s1} \\ 0 & h_{s1} \leq z \leq h_{s1} + g_0 - h_m \\ -k_2(z - h_{s1} - g_0 + h_m) & z > h_{s1} + g_0 - h_m \end{cases} \tag{4.19}$$

To obtain the magnetic field created by the magnet, *COMSOL Multiphysics* software was used. To do so, the *magnetic field, no currents node* within the AC/DC module was used. To model the magnet, a magnetic flux conservation node with a remanent magnetic flux density of 1.3 T corresponding to a Neodymium magnet with an N42 magnetization, was applied to a disk of 15 mm height and 20 mm diameter (the magnet dimensions). Afterwards, a sphere of air of radius 1 m was used as the physical domain, and all the domains were meshed with integrated automatic meshing. The radial component of the magnetic flux density at the average radius of the coil (31.75 mm) was then obtained for different vertical positions (vertical direction is the direction of the magnet movement). The predicted values used in the model are presented in Figure 4.3. The predicted values are fittet with a polynomial of order fifteen to be used in *MATLAB*.

Each of the coils were discretized as ten sub-coils, and the magnetic flux density distribution is used to evaluate the c_{es} and the emf_s as shown in equations 4.20 and 4.21:

$$c_{es} = \frac{B_r^2 l^2}{R_{cs} + R_L} \tag{4.20}$$

$$emf_s = lB_r\dot{z} \tag{4.21}$$

where B_r is the radial component of the magnetic field at the sub-coil, l the length of the copper wire of the sub-coil and R_{cs} is the resistance of the sub-coil. The magnetic flux density at each

sub-coil is evaluated at each time step using the relative position of the magnet and the sub-coil. Then, the c_{es} and the emf_s are calculated for each sub-coil and all the c_{es} are summed to obtain the total c_e while the total emf is calculated as $emf = emf_1 - emf_2 + emf_3$ as coil one is in series, coil two in anti-series and coil three in series.

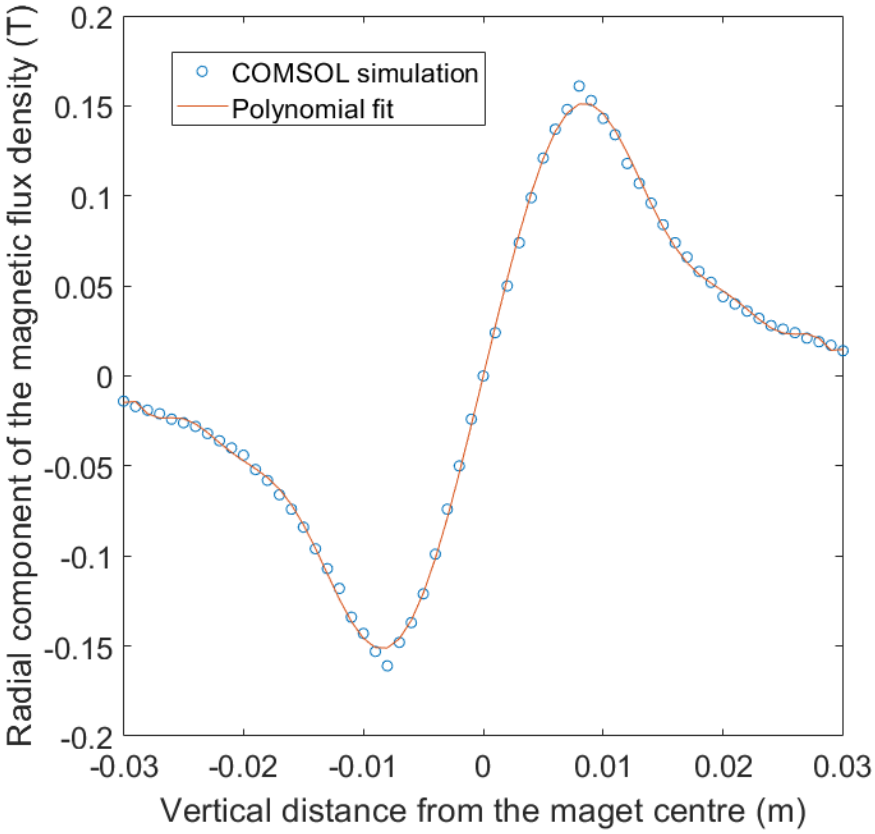

Figure 4.3: *Radial component of the magnetic flux density calculated along a vertical line passing in the middle of the coil width, simulated using COMSOL Multiphysics, and, the polynomial fitted using MATLAB*

To obtain the friction coefficient, a drop test experiment was carried out in which the magnet was dropped into the harvester case and its position was measured as described later in Section 5. Then the results where plotted in *MATLAB* and then an exponential was fitted in order to find the friction coefficient as can be seen in Figure 4.4. The number exponent of the fitting is 2.17 which is the $\gamma/2$ [33]. Because it is known the relation between the damping ratio and the friction coefficient for a viscously damped simple harmonic oscillator is $\gamma = c_{mf}/m$ [33] and the mass of

the magnet is 35.25 g, then the experimental value of the friction coefficient is 0.15.

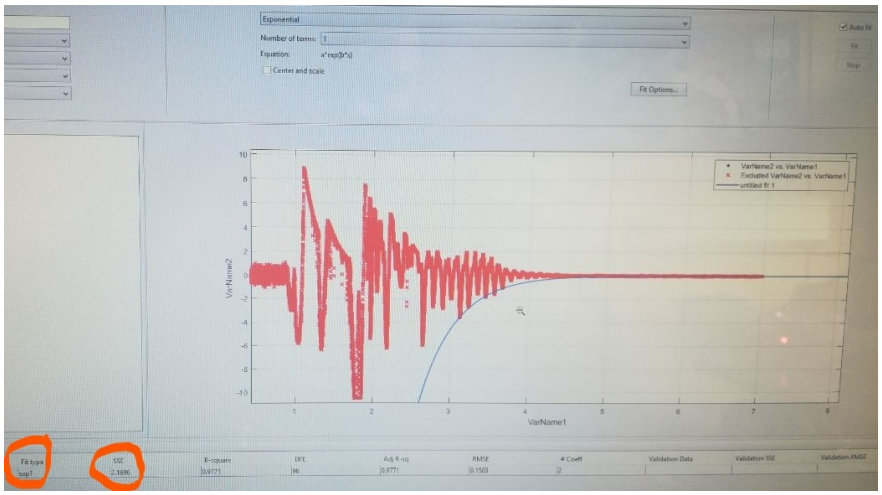

Figure 4.4: *Friction coefficient extracted from the drop test results using an exponential fit.*

Equations 1 to 3 can be solved using the classic Runge–Kutta method, which is a method to integrate first order differential equations over time [34]. In this case u is a matrix containing the main variables (displacement, velocity and voltage) and it is assumed that $du/dt = f(u,t)$. The set of equations for the Runge-Kutta algorithm is:

$$r_{1,i} = f(t_n, u_n)_i \tag{4.22}$$

$$r_{2,i} = f(t_n + \Delta t/2, u_n + \Delta t r_1/2)_i \tag{4.23}$$

$$r_{3,i} = f(t_n + \Delta t/2, u_n + \Delta t r_2/2)_i \tag{4.24}$$

$$r_{4,i} = f(t_n + \Delta t, u_n + \Delta t r_3)_i \tag{4.25}$$

$$u_{n+1,i} = u_{n,i} + \frac{\Delta t}{6}(r_{1,i} + 2r_{2,i} + 2r_{3,i} + r_{4,i}) \tag{4.26}$$

$$t_{n+1,i} = t_{n,i} + \Delta t \tag{4.27}$$

where r are the Runge–Kutta parameters, t is the time, and u is the variable that is integrated. The subscript n indicates the current increment of time, and the subscript i is used to indicate to which

of the three variables (displacement, velocity and voltage) is the Runge–Kutta parameter related to.

Finally, a tuning of the magnetic field and friction coefficient was carried out after the experiments, so the simulation would match the experimental results. In the end, the magnetic field distribution simulated was divided by fifteen, and the c_{mf} was set to 0.12.

4.2 *MATLAB* Code

In this section, the different *MATLAB* scripts used to predict the power output and the frequency response of the energy harvester device are explained in detail.

4.2.1 OneD_NonLinear_Harvester_Main

First of all, all the work-space variables are erased, the figures closed and the command window cleaned. Then the *tic* command is used to time how much time it takes to run the simulation. Then all the input data and variable needed are defined, like the gravity, the geometrical parameters of the harvester, the magnet properties, the coils properties, the load resistance, the spring parameters and the damping coefficients. For the magnetic flux density, the data points from the *COMSOL Multiphysics* simulation are read using the *readtable* command, transformed into two vectors with the command *table2array* and finally a polynomial of order 15 is created (**p**) using the *polyfit* command.

```
clear all
close all
clc
%% Input Data %%
tic

g = 9.81*1; % Gravity acceleration (m/s^2)
%m1 = 5; % Mass of the external device (Kg)
%%%%%%% Geometric Parameters %%%%%%%
hs1 = 19e-3; % Length of the spring 1 (m)
hs2 = 19e-3; % Length of the spring 2 (m)
shs1 = 4e-3; % Solid length of the spring 1 (m)
shs2 = 4e-3; % Solid length of the spring 2 (m)
gap = 16e-3; % Gap between springs (m)
z_0=hs1; % Initial position of the lower part of the magnet (m)

%%%%%%% Magnet Parameters %%%%%%%
m2 = 35.25e-3; % Mass of the magnet (Kg) Haroun
hm = 15e-3; % Length of the magnet (m) Haroun
table=readtable('Magnetic_Flux_Density.txt');
Mag_Flux_Pos=table2array(table(:,1)); % Magnetic field position created by the ...
    magnet (NdFeB 20mm diameter 15mm Length) (m) Simulated using COMSOL
```

```
Mag_Flux_Dens=table2array(table(:,2))/15; % Magnetic field created by the ...
    magnet (NdFeB 20mm diameter 15mm Length) (T) Simulated using COMSOL
p=polyfit(Mag_Flux_Pos,Mag_Flux_Dens,15);
%%%%%%% Coil Parameters and Load %%%%%%%
dw = 0.15e-3; % Diameter of the wire (m)
rc = 25e-3; % Internal radius of the coil (m)
Nr = 25; % Number of turns in the radial direction of the coil
Nz =90; %Number of turns in along the length of the coil
lw = 9*2*pi*Nr*(rc+0.5*Nr*dw); % Length of 9 turns in axial direction of the ...
    coil wire (m)
%Rc = 0.01694e-6*lw/(pi*(dw/2)^2); % Coil resistance (ohm)
Rc = 893/3; % Coil resistance (ohm) Exp Value
Lc = 3*(0.8*(rc+dw*Nr/2)^2*Nz^2/(0.0254*...
(6*(rc+dw*Nr/2)+9*dw*Nz+10*dw*Nr)))*1e-6; % Coil Inductance (H)
RL = Rc*3; % Load resistance (ohm)

% Coil sections below are the ones that the model work for, but I made a
% mistake and there are 11 sections and the lw is the one for a section
% when the coil is divided in 10 sections.
Coil_Section1=[0:9*dw:dw*Nz];
Coil_Section2=[dw*Nz:9*dw:2*dw*Nz];
Coil_Section3=[2*dw*Nz:9*dw:3*dw*Nz];
% Coil_Section1=[9*dw/2:9*dw:dw*(Nz)-9*dw/2];
% Coil_Section2=[dw*Nz+9*dw/2:9*dw:2*dw*Nz-9*dw/2];
% Coil_Section3=[2*dw*Nz+9*dw/2:9*dw:3*dw*Nz-9*dw/2];

%%%%%%% Stiffness and Damping Parameters %%%%%%%
k1 = 115; % Stiffness of spring 1 (N/m)
k2 = 115; % Stiffness of spring 2 (N/m)
cmf = 0.12; % Damping coefficient of air + friction (N/ms) Experimental 0.15
cms1 = 0; % Extra damping coefficient due to contact with spring 1 (N/ms)
cms2 = 0; % Extra damping coefficient due to contact with spring 2 (N/ms)
% ce is Electromagnetic damping aproximation (N/ms)
% emf_v is Electromotive force divided the velocity(V)
```

Then the numerical sampling frequency parameters are defined, which define the time-step (**dt**) that will be used throughout the simulation. A numerical sampling frequency (**Fs**) of at least 10^6 Hz is needed in order to avoid divergence. The power variable (**Pow**) is initialized to optimise the program. the Total time simulated (**tfin**) is also defined. Then two loops and loop variables are defined in order to run the simulation for multiple parameters, like external frequencies, friction coefficients, load resistances, etc. In the specific case below, for three different gaps between springs (first *for*), it runs the simulation for thirteen different external frequencies (second *for*).

```
%%%%%%% Sampling Frequency Parameters %%%%%%%
Fs=1e6; % Numerical sampling frequency (Hz)
dt=1/Fs; % Increment of time (s)
tin=0; % Initial time (s)
tfin=4; % Final time (s)
t=tin:dt:tfin; % Time vector (s)
L=length(t); % Length of the vectors
magfield=zeros(1,L);

%%%%% Loop Variables %%%%
%variable=[7:0.5:10];
variable=[6:0.5:12];
%variable=8.5;
%variable2=[0.05:0.05:0.2];
variable2=[16e-3,18e-3,20e-3];
%variable2=0.12;

Pow=zeros(length(variable),length(variable2));


for x=1:length(variable2)
gap=variable2(x);
%cmf=variable2(x);
%%%%%%% Input Vibration Parameters %%%%%%%
freq=9; % Frequency of the input motion (Hz)

for i=1:length(variable)
freq=variable(i);
```

In the lines below the input acceleration (which has a sinusoidal form) is defined creating a vector with a sinusoidal wave (**a1**) with a frequency equal to the external frequency and amplitude equal to 1 with the command *gensig*. The it is multiplied by $\sqrt{2}$ times the target rms acceleration (**rms_acc**) to obtain the input acceleration with the command **a**. Then the output variables (**u**) are initialised for the case of the magnet starting on top of the bottom spring in a rest state. **u(1,1)** refers to the initial position of the magnet, **u(1,2)** refers to the initial velocity of the magnet and **u(1,3)** refers to the initial voltage at the load resistance.

```
rms_acc=0.5;% Rms input acceleration (g)
acc=rms_acc*sqrt(2)*9.81; % Maximum of the input acceleration (m/s^2)
Y = acc/((2*pi*freq)^2); % Amplitude of the input motion (m)
a1=gensig('sin',1/freq,tfin,dt); % It generates a sinusoidal signal of ...
    frequency freq
a=acc*a1;% Input acceleration (m/s^2)
% The vibration will have sinusoidal form y(t) = Y*sin(2*pi*f*t)


%% Classic Runge-Kutta "RK4" %%
u=zeros(L,3); % initialisation of the vector u with the solutions, u(:,1) is ...
    the position of the lower part of the magnet; u(:,2) is the velocity; u(:,3) ...
    is the voltage
u(1,1)=z_0; %Initial position of the simulation (m)
u(1,2)=0; % Initial velocity of the simulation (m/s)
u(1,3)=0; % Initial voltage of the simulation (V)
```

Now the simulation part comes. A *for* of length equal to the length of the time vector (which will be the number of time-steps simulated) starts. Inside it, for every time-step, first the electromagnetic damping (**ce**) and the electromotive force(divided the velocity) (**emf_v**) generated are calculated using the function *Equivalent_Magnetic_Field*. Next, the four different Runge-Kutta parameters (**k41, k42, k43, k44**) are calculated using the function *Runge_Kutta_Harvester _velo*. Once all the parameters are calculated using the variables of the previous time-step, the current time-step output variables are calculated using Equation 4.26. In the *if* below are used in the event of the magnet reaching a position where either of the springs can not compress anymore (the solid heights of the springs). What happens then is that the position of the magnet is set to the one of the solid height of the springs, and the direction of the velocity is inverted and multiplied by a factor of 0.9.

```
for j=1:(L-1)

     [ce,emf_v]=Equivalent_Magnetic_Field(...
u(j,1),lw,Rc,RL,Coil_Section1,Coil_Section2,Coil_Section3,p);
     k41 = Runge_Kutta_Harvester_velo(u(j,:),a(j),hs1...
,gap,hm,m2,cmf,cms1,cms2,Rc,RL,Lc,g,k1,k2,ce,emf_v);
     k42 = Runge_Kutta_Harvester_velo(u(j,:)+dt/2*k41(1,:),a(j),...
hs1,gap,hm,m2,cmf,cms1,cms2,Rc,RL,Lc,g,k1,k2,ce,emf_v);
     k43 = Runge_Kutta_Harvester_velo(u(j,:)+dt/2*k42(1,:),a(j),...
hs1,gap,hm,m2,cmf,cms1,cms2,Rc,RL,Lc,g,k1,k2,ce,emf_v);
     k44 = Runge_Kutta_Harvester_velo(u(j,:)+dt*k43(1,:),a(j),...
hs1,gap,hm,m2,cmf,cms1,cms2,Rc,RL,Lc,g,k1,k2,ce,emf_v);
     u(j+1,:)=u(j,:)+dt/6*(k41(1,:)+2*k42(1,:)+2*k43(1,:)+k44(1,:));
     if u(j+1,1)<shs1 % Elastic shock at the bottom spring
         u(j+1,1)=shs1;
         u(j+1,2)=-u(j+1,2)*0.9;
```

```
17        elseif u(j+1,1)>hs1+gap-hm+hs2-shs2 % Elastic shock at the top spring
18            u(j+1,1)=hs1+gap-hm+hs2-shs2;
19            u(j+1,2)=-u(j+1,2)*0.9;
20        end
21    end
```

Finally the rms voltage (**Vrms**) is calculated using the voltage values of the last seconds of the simulation (where the motion is already stable) with the command *rms*. Then the rms output power (**Pow**) is calculated as $P_{rms} = V_{rms}^2/R_L$. To finish, the rms output power is plotted against the loop variable 1 and then the *toc* is used to finish the time count started by *tic*.

```
1  V=u(tfin/dt-1/dt:tfin/dt+1,3); % The voltage used for the rms voltage is the ...
       one after the system is stable
2  Vrms = rms(V); % Calculates the rms of the voltage across the load resistance (V)
3  Pow(i,x)= Vrms^2/RL; % Calculates the power harvester (W)
4  end
5
6    figure
7    plot(variable,Pow(:,x)*1000,'-*')
8  end
9  toc
```

4.2.2 Equivalent_Magnetic_Field

The first thing done is to define the function name, outputs and inputs. Then the relative position between the magnet and the sub-coils (**Rel_Pos**) is calculated subtracting the magnet position (**u**) to each of the sub-coil centres (**Coil_Section**). Next the variables for the differential electromagnetic damping (**dce**) and electromotive force(divided the velocity) (**demf**) for each coil are initialised, and the number of sub-coils per section is calculated using the command *length*.

```
1  function [ce,emf_v]=Equivalent_Magnetic_Field(...
2  u,lw,Rc,RL,Coil_Section1,Coil_Section2,Coil_Section3,p)
3      Rel_Pos1=Coil_Section1-u; %relative position of the magnet centre with the ...
           coil sections
4      Rel_Pos2=Coil_Section2-u;
5      Rel_Pos3=Coil_Section3-u;
6      dce1=0;
7      dce2=0;
8      dce3=0;
9      demf1=0;
10     demf2=0;
11     demf3=0;
12     n=length(Coil_Section1);
```

Now a loop to calculate the total electromagnetic damping caused by the coils to the magnet and the total electromotive force created at the coils. If the value of the sub-coil relative position, if it is between 0.03 and -0.03, then the magnetic field at that position (**Temp_Mag_Flux_Dens**) is calculated using the fifteen order polynomial using the command *polyval*. If the relative position is outside the limits stated above, the magnetic field is considered zero. The electromagnetic damping of each sub-coil is calculated with Equation 4.20 and the electromotive force of each-coil as in Equation 4.21 but omitting the velocity term. Then, to obtain the total values of each coil, the values of each sub-coils are added to the values of the previous sub-coils. Finally, the c_es of each coil are summed to obtain the total c_e (**ce**) while the total emf (**emf_v**) is calculated as $emf_v = demf1 - demf2 + demf3$ as explained in the previously.

```
1       for i=1:n %loop to calculate the emf and ce of each section
2
3           pos1=Rel_Pos1(i);
4           pos2=Rel_Pos2(i);
5           pos3=Rel_Pos3(i);
6           % when the coil is further than +-0.03m from the magnet center, the
7           % magnetic fiels is considered 0
8           %Coil 1
9           if pos1<-0.03
10
11
12          elseif pos1>0.03
13
14
15          else
16              Temp_Mag_Flux_Dens=polyval(p,pos1);
17              dce1=dce1+Temp_Mag_Flux_Dens^2*lw^2/(Rc/n+RL);
18              demf1=demf1+Temp_Mag_Flux_Dens*lw;
19          end
20
21          %Coil2
22          if pos2<-0.03
23
24
25          elseif pos2>0.03
26
27
28          else
29              Temp_Mag_Flux_Dens=polyval(p,pos2);
30              dce2=dce2+Temp_Mag_Flux_Dens^2*lw^2/(Rc/n+RL);
31              demf2=demf2+Temp_Mag_Flux_Dens*lw;
32          end
33
34          %Coil3
35          if pos3<-0.03
36
```

```
37
38          elseif pos3>0.03
39
40
41          else
42              Temp_Mag_Flux_Dens=polyval(p,pos3);
43              dce3=dce3+Temp_Mag_Flux_Dens^2*lw^2/(Rc/n+RL);
44              demf3=demf3+Temp_Mag_Flux_Dens*lw;
45          end
46      end
47      ce=dce1+dce2+dce3;
48      emf_v=demf1-demf2+demf3;
49  end
```

4.2.3 Runge_Kutta_Harvester_velo

This function is where the 3 differential equations are solved for each time-step. As in the previous function, at the beginning the the function name, outputs and inputs are defined. Depending on the magnet position, one set of equations or another are used, with the only difference among them being the elastic force term. The corresponding damping and elastic force are assigned and then each equation is solved using the input values. In this function A, B and C are $\dot{z}$, $\dot{v}$ and $\dot{V_L}$ respectively.

```
1  function f1=Runge_Kutta_Harvester_velo(...
2  u,a,hs1,gap,hm,m2,cmf,cms1,cms2,Rc,RL,Lc,g,k1,k2,ce,emf_v)
3  % Properties of the system when the magnet touches spring 1
4  if u(1)≤hs1 %z=0 is at the bottom of the bottom spring
5      d=cmf+cms1; % Damping due to friction+air+spring
6      k=k1; % Spring 1 force
7      A=u(2); % This represents dz/dt = u(2). It is needed because the original ...
           eq is a second order equation
8      B=(-d*u(2)-k*(u(1)-hs1)-ce*u(2)+m2*a-m2*g)/m2; % this is basically the ...
           equation to solve but dz/dt = u(2)
9      C=emf_v*RL*u(2)/Lc-(RL+Rc)*u(3)/Lc; %this is the voltage equation
10     f1=[A,B,C];
11
12 % Properties of the system when the magnet touches spring 2
13 elseif u(1)≥hs1+gap-hm %z=0 is at the bottom of the bottom spring
14     d=cmf+cms2; % Damping due to friction+air+spring
15     k=k2; % Spring 2 force
16     A=u(2);
17     B=(-d*u(2)-k*(u(1)-(hs1+gap-hm))-ce*u(2)+m2*a-m2*g)/m2;
18     C=emf_v*RL*u(2)/Lc-(RL+Rc)*u(3)/Lc;
19     f1=[A,B,C];
20
21 % Properties of the system when the magnet is between springs
```

```
22 elseif u(1)>hs1 && u(1)<hs1+gap-hm %z=0 is at the bottom of the bottom spring
23     d=cmf; % Damping only due to friction and air
24     k=0; % No spring force
25     A=u(2);
26     B=(-d*u(2)-ce*u(2)+m2*a-m2*g)/m2;
27     C=emf_v*RL*u(2)/Lc-(RL+Rc)*u(3)/Lc;
28     f1=[A,B,C];
29 end
30
31 end
```

5 EXPERIMENTAL VALIDATION

To validate the model results, a prototype harvester was tested. The main monitored variable was the output power. In this section, the harvester used for the experiments is described, as well as the methodology and the set up for the experiments. In chapter 6, the experimental results are presented and then compared with the predictions of the model.

5.1 Device

In order to obtain data to validate the model and also to prove the working principle of the harvester, a prototype of the harvester was designed and built. A schematic of the harvester and its parts is presented in Figure 5.1.

The device consists of a 3D printed case that is attached to the shaker by means of screws. In the lower part of the case, there is space to place an accelerometer. The accelerometer is placed in the lower part of the case to avoid as much as possible the interference cause by small movement of all the screwed parts. The case also accommodates a teflon tube (to achieve a low c_{mf}) with up to six copper coils around it (only 3 where used for the experiment as the tested distances between springs were less than the height of 3 coils). Inside the teflon tube there is the moving mass (a magnet). On the bottom there is a spring attached to the case, and on the top there is one attached to the case. The cap can be moved in order to change the distance between the springs and thus the free motion length (g_0). The top part has a hole in the middle that goes through all the cap, to let a laser beam of the laser displacement gauge pass through and record the position of the magnet.

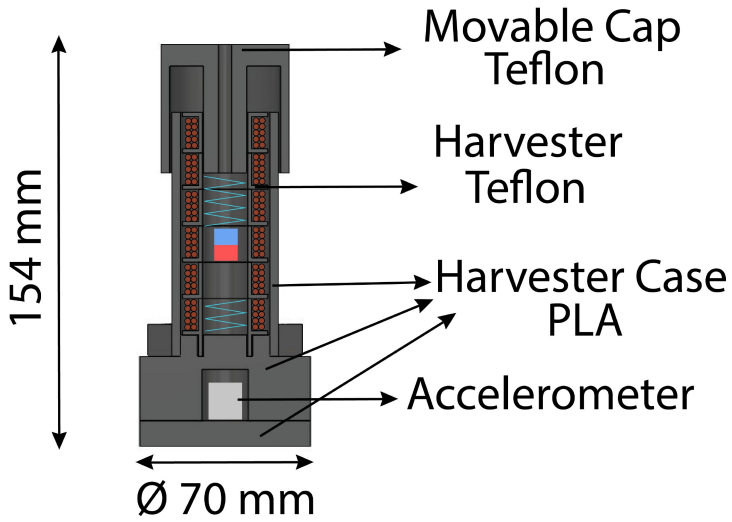

Figure 5.1: *Prototype of the harvester designed and built to obtain experimental data.*

To coil the copper coils around the teflon case, an automatic coiling machine (CNC design ltd 2018 Coil W) was used. The controller of the machine (Coil Winder ARM Controller MKII Software V1.7) only needed as an input the number of turns in the axial and radial direction as well as the turn velocity. A test was done before coiling to observe that with the input angular velocity, the coiling has no appreciable imperfections. In Figure 5.2, the set up is presented.

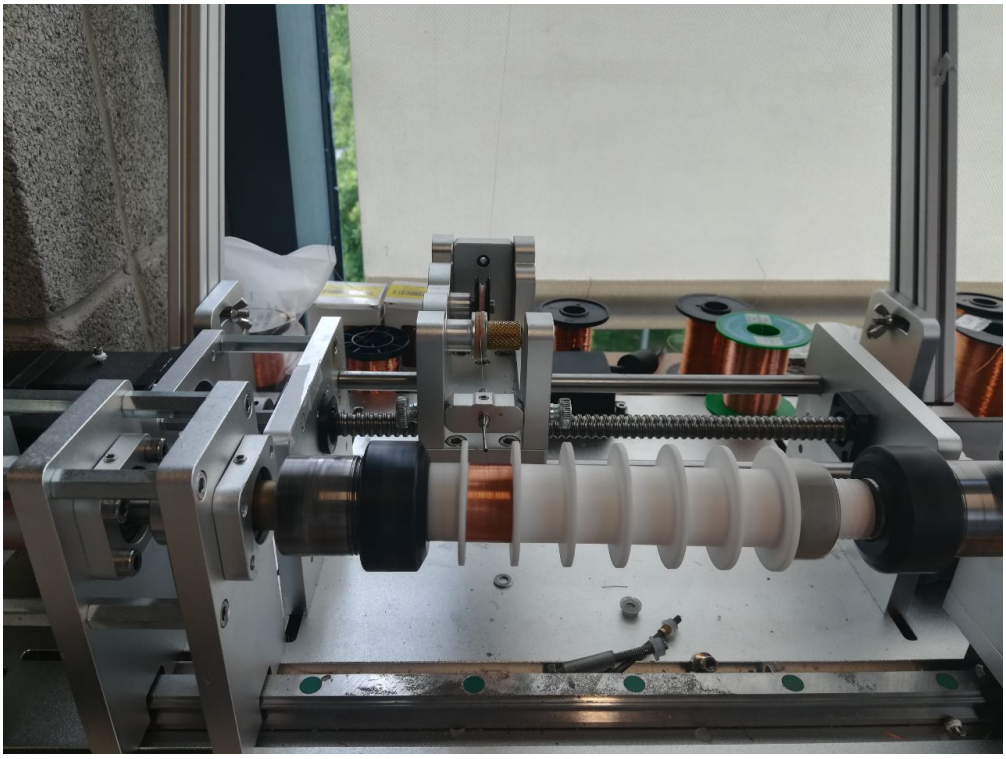

Figure 5.2: *Coiling set up.*

5.2 Experimental Set Up and Methodology

The main variables that were monitored are the output voltage across the load resistance (to obtain later the root-mean-squared -rms- power produced by the harvester), the input acceleration (to know the conditions at which the harvester was working), and the displacement of the shaker (to avoid surpassing the maximum recommended displacement). A schematic of the experimental set up can be seen in Figure 5.3.

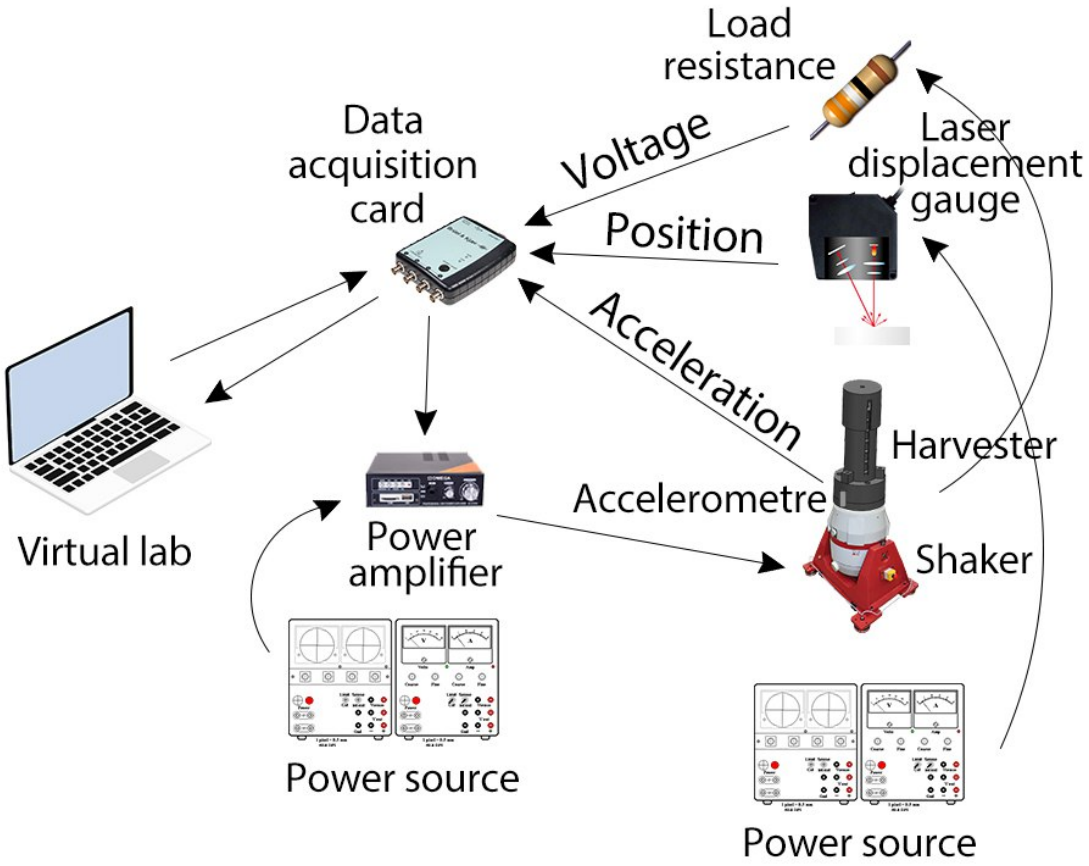

Figure 5.3: *Schematic of the experimental set up with all the relevant elements used during the experiments.*

The harvester device was connected to the shaker by means of screws, and the accelerometer was glued in the lower part of the harvester. The coils of the harvester were connected in a series, anti-series, series schematic among themselves and to a resistance decade box that acted as the load resistance. A laser displacement gauge was used to measure the displacement of the top of the device. A data acquisition card and *LabVIEW* were used to read and save the data coming from the accelerometer, load resistance and laser displacement gauge. *LabVIEW* was also used to create the sine wave that made the shaker vibrate. The signal from the computer went to the data acquisition card, and from there to a power amplifier. The acceleration generated by the shaker was controlled and changed by varying the gain of the power amplifier. A list of the suppliers and models of the lab equipment is found in Table 5.1.

Device	Model	Supplier
Power supply 1	*E362A*	*Keysight*
Power supply 2	*EL302D*	*TTI -Thurlby Thandar Instruments*
Data acquisition card	*USB-4431*	*NI*
LabVIEW	*2011*	*NI*
Laser displacement gauge	*Opto NCDT LD 1607-20*	*Micro-epsilon*
Shaker	*V406*	*LDS*
Accelerometer	*353B51*	*PCB Piezotronics*
Resistance decade box	*DR07*	*ELC*
Power amplifier	*MA-150*	*Kinter*

Table 5.1: *Model and supplier of all the lab equipment used in the experiments.*

Using the power amplifier and *LabVIEW*, the input acceleration was manually adjusted to the desired one ($0.2g$ and $0.5g$ were the tested rms accelerations) and the resistance decade box that acted as a load resistance was set to 893 Ω. The range of frequencies studied was 6 Hz to 12 Hz in increments of 0.5 Hz. For each frequency, the harvester started from rest, and the data was taken when the harvester was in a stable motion. The data acquisition was repeated twice for every input frequency and acceleration. This was done for two reasons, one to check that the data obtained was very similar (and this way help to detect possible errors) and to obtain an average power for each experiment. This procedure was repeated for three different gaps between springs (16 mm, 18 mm, 20 mm,). All the data was then saved inside a .txt file and then post processed with *MATLAB*. In Figure 5.4 a photo of the experimental setup in the laboratory can be found.

Another experiment was carried out, in which the output power at the load resistance was monitored for different load resistances to find the optimal load resistance for a configuration with only one spring in the bottom part (free end in the top). The input frequency was 8.5 Hz and the rms acceleration was $0.2g$. For other configurations, the experiment should be repeated to see if the behaviour stays the same when varying the input frequency or rms acceleration.
A drop test was also carried out in order to find the friction coefficient. The test consisted in dropping the magnet inside the case (where it usually oscillates) and measure its position with the laser displacement gauge while it oscillated freely around the bottom spring. The harvester had to be in a vertical position to reproduce the test conditions, and the coils had to be in open circuit so there was no electromagnetic damping involved. Once the data was saved, an exponential was fitted to the harmonic oscillation of the magnet in the drop test. The friction coefficient calculated as described in the previous chapter was found to be 0.15.

Figure 5.4: *Photo of the experimental setup in the laboratory.*

5.3 Limitations and Problems of the Experiments

During the experiments, some limitations were encountered, which are listed below:

- The experiment could not achieved less than 6 Hz (5 Hz is the lower limit) and more than 1 g could not be applied, to protect the shaker from overloading.
- The equipment was that it could not recreate the circular motion of a wind turbine blade, so the effect of the gravity and centrifugal forces acting in different directions relative to the harvester movement was omitted from the study. The change of direction of gravity relative to the magnet motion might have an influence on the dynamic behaviour of the harvester, and thus to its resonance frequency, and should be studied in further work.
- The space needed for the laser displacement gauge to work appropriately was bigger then the hole in the cap (which was the same diameter as the springs inside) so the position of magnet during the validation tests could not be recorded. This was a minor problem as the variable used to validate the model was the rms output power and the recording of the position was

supposed to be more of a tool to help find what could not be working in the model comparing the predicted and the measured displacement.

- The mass of the magnet was quite big and was producing appreciable impacts on the shaker for $0.2g$, which produced peaks on the acceleration reading that affected the calculations of the rms acceleration. This could have been solved by adding mass to the case, but the shaker was not quite powerful and with a significant increment of mass on the shaker, it would have had problems delivering the desired output accelerations.

6 RESULTS

In this section, the results obtained from the experiments are presented and compared to the ones obtained from the model. Afterwards, a discussion on what the results mean and how well the model agrees with the experimented is provided.

The results of the experiments and the predicted values are presented in Figures 6.1 and 6.2 for the output rms power as a function of frequency for different g_0 for rms acceleration of 0.2 g and 0.5 g. Figure 6.3 shows the experimental rms output power as a function of R_L for an rms acceleration of 0.2 g is presented.

The experiments show that an increase in the gap between the two springs (from 16 mm to 20 mm) results in a change of the natural frequency of $-1Hz$, with only a decrease in power of 1.53 mW to 1.27 mW for an rms acceleration of 0.2 g and of 2.28 mW to 1.59 mW for an rms acceleration of 0.5 g. This effect persists when the input acceleration changes, for values < 1 g. The model predicts with accuracy the frequency shift, and predicts the power output for an rms acceleration of 0.2 g with a deviation of 29%, and for an rms acceleration of 0.5 g with a deviation of -22%. The prototype was not optimize, which means the harvester has potential to generate more power if optimised. A linear spring-mass featuring the same spring constant and mass of the prototype has a natural frequency of 9.1 Hz. Table 6.1 presents a summary of the results.

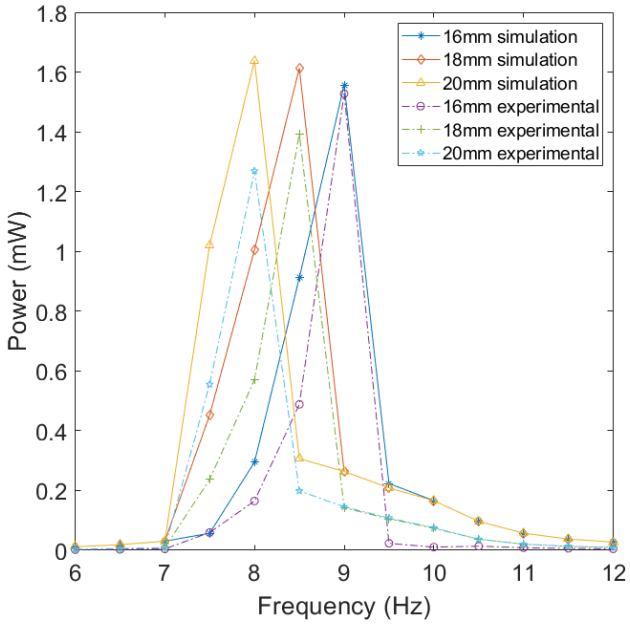

Figure 6.1: *Experimental and predicted rms power output against frequency for* 0.2 g *rms acceleration and* 893Ω *load resistance for different gaps between springs.*

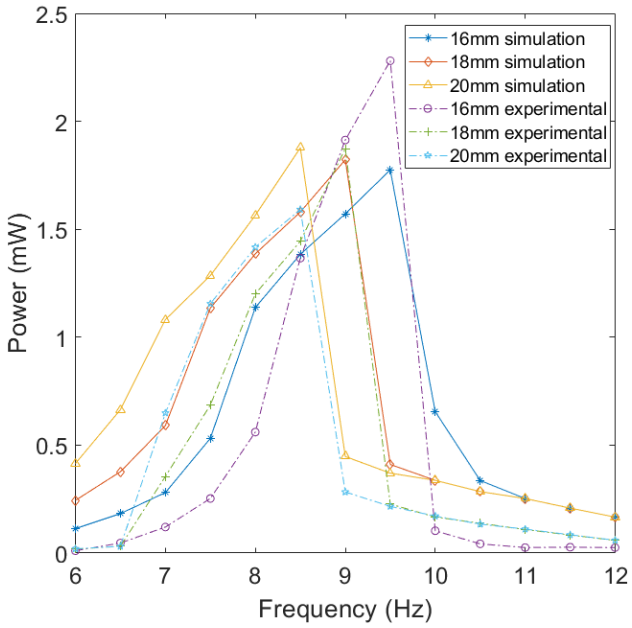

Figure 6.2: *Experimental and predicted rms power output against frequency for* 0.5 g *rms acceleration and* 893 Ω *load resistance for different gaps between springs.*

		Experimental values				
Predicted values						
Rms acc (g)	g_0 (mm)	Max rms power (mW)	Ressonance frequency (Hz)	Bandwidth (Hz)	Max rms power (mW)	Ressonance frequency (Hz)
0.2	16	1.53	9.0	0.61	1.56	9.0
0.2	18	1.39	8.5	0.70	1.61	8.5
0.2	20	1.27	8.0	0.73	1.64	8.0
0.5	16	2.28	9.5	1.42	1.78	9.5
0.5	18	1.87	9.0	1.56	1.82	9.0
0.5	20	1.59	8.5	1.70	1.88	8.5

Table 6.1: *Experimental and predicted rms power output, resonance frequency and bandwidth for different conditions.*

An important point to note is the fact that for 0.5 g, when the harvester approached the natural frequency from the low frequency side, the magnet was having strong impacts against the case, which produced peaks in the acceleration readings. This lead to a less accurate control of the rms acceleration. The order of the power is of mW, which is a good sign that even if harvester is optimised for a low frequency, it can achieve the target power of 5.5 mW.

The results of the load resistance study show that there is not much difference between 700 Ω and 1100 Ω. The fluctuations in that range are are believed to be a result of the human error when selecting the input acceleration. The fact that part of the curve is quite flat, makes the small errors in setting the input acceleration more visible.

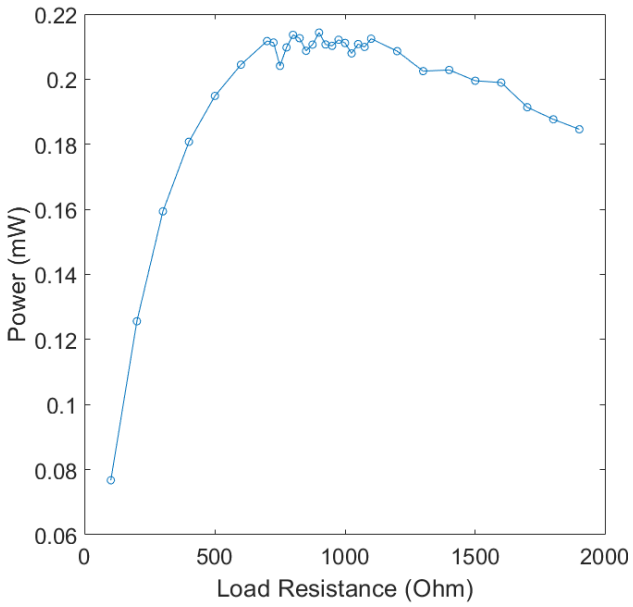

Figure 6.3: *Experimental results of the rms power output for different load resistances for* 8.5 Hz, 0.2 g *rms acceleration, and the free end configuration (only bottom spring).*

7 CONCLUSIONS

An electromagnetic vibrational energy harvester suitable for powering sensors located on the blades of a wind turbine was designed, modelled and tested experimentally. In this section, the main conclusions of this paper are presented. After the simulation, the experiments and the tuning of the model the main conclusions of this report are:

- Experimentally, it was observed that the resonant frequency shifted to lower values when the distance between the springs is increased. When the gap between the springs is increased from 16 mm to 20 mm, at an rms acceleration of 0.2 g, the resonance shifted from 9 Hz to 8 Hz. The power generated with a 893 Ω load resistance went from 1.53 mW to 1.27 mW, respectively. For the same gap increase and load resistance, at an rms acceleration of 0.5 g the resonant peak shifted from 9.5 Hz to 8.5 Hz and the power generated went from 2.28 mW to 1.59 mW respectively. If optimised, the harvester has the potential to generate the target current of 5.5 mW.

- The experiments show that the max bandwidth of the prototype harvester is 73 Hz for 0.2 g rms acceleration and 1.7 Hz for 0.5 g rms acceleration.

- After tuned, the model successfully predicts the frequency shift and the output rms power when changing distance between the top and the bottom springs. It predicts the rms power output with a maximum error of 29% for 0.2 g rms acceleration and -22% for 0.5 g rms acceleration for a distance between springs of 20 mm. This is because the model was tuned to match perfectly at the conditions of 0.2 g rms acceleration and 16 mm distance between springs. As the distance between spring increases, the discrepancy increases.

- Although the experimental results show a decrease in the rms power when increasing the the distance between the top and the bottom spring, the model predicts an increase in the rms power.

This report has demonstrated that the chosen harvesting technology has the potential to generate enough energy to power small sensors from the typical low frequency vibrations present on the tip of a wind turbine blade. Furthermore, the model could be used to predict the behaviour of the non-linear one degree-of-freedom mass-spring harvester and to optimise geometrical parameters to the desired working conditions.

8 RECOMMENDATIONS FOR FUTURE WORK

Further work on the modelling assumptions can be carried out, in order to improve the accuracy of the model. The next steps on this project should focus on:

- Study the effects of forces product of rotation on the harvester dynamics when rotational motion is considered.
- Optimization of the following parameters: number of sub-coils, mass of the magnet, elastic constant, and the magnetic field fit.
- Improve the friction modelling by taking into account extra friction coefficients when the magnet is in contact with the springs.
- Measure the coil inductance experimentally.
- Carry out a parameter study of the magnetic field and the friction coefficients in order to match them to the experimental results.
- Carry out experiments to see how the optimum load resistance changes when changing the distance between springs or the input acceleration.
- The fact that an increase on the distance between the top and the bottom spring lowers the natural frequency with a relatively small power decrease, means that some kind of mechanical control could be implemented to change this distance depending on the external frequency and, thus, give the harvester a wider range of operation.

Acknowledgments

I would like to thank Dr. Valeria Nico and Dr. Jeff Punch for their counsel and assistance throughout the project. I would also like to thank Dr. Daniel Garcia-Almiñana for his guidance in the writing of this project. Finally, I would like to thank Mireia Graells Sendrós for helping me with the figures of the paper and supporting me through the project.

Bibliography

[1] D. Fang and J. Liu, *Fracture Mechanics of Piezoelectric and Ferroelectric Solids*, T. U. Press, Ed. Beijing: Springer, 2013.

[2] P. A. Tipler and G. Mosca, *Física para la ciencia y la tecnologia*, 6th ed., Reverté, Ed. Barcelona: Reverté, 2010, vol. 2.

[3] K. I. Lee, B. J. Lim, S. H. Kim, and Y. Hong, "Energy harvesting by rotation of wheel for tire monitoring system," *SENSORS, 2012 IEEE*, pp. 1–4, 2012.

[4] T. Toh, A. Bansal, G. Hong, P. Mitcheson, A. Holmes, and E. Yeatman, "Energy harvesting from rotating structures," *Proceedings of PowerMEMS 2007, Nov 28 - 29, Freiburg, Germany*, pp. 327–330, 2007.

[5] M. Febbo, S. P. Machado, J. M. Ramirez, and C. D. Gatti, "A low frequency rotational energy harvesting system," *Journal of Physics: Conference Series*, vol. 773, p. 12058, 11 2016. [Online]. Available: https://doi.org/10.1088%2F1742-6596%2F773%2F1%2F012058

[6] L. Gu and C. Livermore, "Compact passively self-tuning energy harvesting for rotating applications," *Smart Materials and Structures*, vol. 21, p. 15002, 12 2011. [Online]. Available: https://doi.org/10.1088%2F0964-1726%2F21%2F1%2F015002

[7] X. Mei, S. Zhou, Z. Yang, T. Kaizuka, and K. Nakano, "The benefits of an asymmetric tri-stable energy harvester in low-frequency rotational motion," *Applied Physics Express*, vol. 12, p. 57002, 4 2019. [Online]. Available: https://doi.org/10.7567%2F1882-0786%2Fab0b75

[8] H. Fu and E. M. Yeatman, "A methodology for low-speed broadband rotational energy harvesting using piezoelectric transduction and frequency up-conversion," *Energy*, vol. 125, pp. 152 – 161, 2017. [Online]. Available: http://www.sciencedirect.com/science/article/pii/S0360544217302979

[9] W.-H. Wu, K.-C. Kuo, Y.-H. Lin, and Y.-C. Tsai, "Non-contact magnetic cantilever-type piezoelectric energy harvester for rotational mechanism," *Microelectronic Engineering*, vol. 191, pp. 16 – 19, 2018. [Online]. Available: http://www.sciencedirect.com/science/article/pii/S0167931718300431

[10] J. M. Ramírez, C. D. Gatti, S. P. Machado, and M. Febbo, "Energy harvesting for autonomous thermal sensing using a linked e-shape multi-beam piezoelectric device in a low frequency rotational motion," *Mechanical Systems and Signal Processing*, vol. 133, p. 106267, 2019. [Online]. Available: http://www.sciencedirect.com/science/article/pii/S0888327019304820

[11] A. Haroun, I. Yamada, and S. Warisawa, "Study of electromagnetic vibration energy harvesting with free/impact motion for low frequency operation," *Journal of Sound and Vibration*, vol. 349, pp. 389 – 402, 2015. [Online]. Available: http://www.sciencedirect.com/science/article/pii/S0022460X15002874

[12] M. A. Halim, R. Rantz, Q. Zhang, L. Gu, K. Yang, and S. Roundy, "An electromagnetic rotational energy harvester using sprung eccentric rotor, driven by pseudo-walking motion," *Applied Energy*, vol. 217, pp. 66 – 74, 2018. [Online]. Available: http://www.sciencedirect.com/science/article/pii/S0306261918302186

[13] K. Ashraf, M. H. M. Khir, J. O. Dennis, and Z. Baharudin, "Improved energy harvesting from low frequency vibrations by resonance amplification at multiple frequencies," *Sensors and Actuators A: Physical*, vol. 195, pp. 123 – 132, 2013. [Online]. Available: http://www.sciencedirect.com/science/article/pii/S092442471300143X

[14] V. Nico, E. Boco, R. Frizzell, and J. Punch, "A high figure of merit vibrational energy harvester for low frequency applications," *Applied Physics Letters*, vol. 108, p. 13902, 2016. [Online]. Available: https://doi.org/10.1063/1.4939545

[15] C. Wang, Q. Zhang, and W. Wang, "Low-frequency wideband vibration energy harvesting by using frequency up-conversion and quin-stable nonlinearity," *Journal of Sound and Vibration*, vol. 399, pp. 169–181, 2017. [Online]. Available: http://www.sciencedirect.com/science/article/pii/S0022460X17301645

[16] T. Liu and C. Livermore, "A compact architecture for passively-switched energy harvesters," *Journal of Physics: Conference Series*, vol. 660, p. 12090, 12 2015. [Online]. Available: https://doi.org/10.1088%2F1742-6596%2F660%2F1%2F012090

[17] K. Fan, Q. Tan, H. Liu, Y. Zhang, and M. Cai, "Improved energy harvesting from low-frequency small vibrations through a monostable piezoelectric energy harvester," *Mechanical Systems and Signal Processing*, vol. 117, pp. 594 – 608, 2019. [Online]. Available: http://www.sciencedirect.com/science/article/pii/S0888327018304679

[18] A. Dewan, S. U. Ay, M. N. Karim, and H. Beyenal, "Alternative power sources for remote sensors: A review," *Journal of Power Sources*, vol. 245, pp. 129–143, 2014.

[19] D. Laun, J. Zhanf, and R. Wang, *Piezoelectric transducer and piezoelectric transducer array*, revised edition ed., B. U. Press, Ed. Beijing: Beijing University Press, 2005.

[20] Q.-M. Wang, *Introduction to Electromechanical Sensors and Actuators*. Pittsburgh: University of Pittsburgh, 2016.

[21] B. D. Wedlock, *Properties of Piezoelectric Materials*. United States Army, 1964.

[22] L. Mateu and F. Moll, "Review of energy harvesting techniques and applications for microelectronics," *VLSI Circuits and Systems II*, vol. 5837, p. 359 – 373, 2005. [Online]. Available: https://doi.org/10.1117/12.613046

[23] Y. Jiang, W. Finnegan, A. Kazemi, P. Meier, and J. Fagan, E. ad Goggins, "Natural frequency measurement of a 13-meter wind turbine blade using different techniques," *Civil Engineering Research Ireland 2020*, 2020.

[24] D. Ju and Q. Sun, "Wind turbine blade flapwise vibration control through input shaping," *Proceedings of the 19th World Congress The International Federation of Automatic Control Cape Town, South Africa, 24-29 August*, 2014.

[25] R. Osgood, "Dynamic characterization testing of wind turbines," *National Renewable Energy Laboratory (Midwest Research Institute)*, 2001.

[26] P. J. Schubel and R. J. Crossley, "Wind turbine blade design," *Energies*, vol. 5, pp. 3425–3449, 9 2012. [Online]. Available: http://www.mdpi.com/1996-1073/5/9/3425

[27] E. Hau, *Wind Turbines: Fundamentals, Technologies, Application, Economics*, 3rd ed. Springer-Verlag, 2013.

[28] R. Fischer, "Aerosense: A self-sustaining wireless sensor node for pressure and acoustic monitoring on wind turbines," *University of Limerick*, 2020.

[29] H. Broen and O. Jesper, "Applied modal analysis of wind turbine blades," *Risø National Laboratory*, 2003.

[30] C. R. Bowen and M. H. Arafa, "Energy harvesting technologies for tire pressure monitoring systems," *Advanced Energy Materials*, vol. 5, p. 1401787, 2015. [Online]. Available: https://onlinelibrary.wiley.com/doi/abs/10.1002/aenm.201401787

[31] Q. Zhao, Y. Liu, L. Wang, H. Yang, and D. Cao, "Design method for piezoelectric cantilever beam structure under low frequency condition," *International Journal of Pavement Research and Technology*, vol. 11, pp. 153 – 159, 2018, in Honor of Professor James S. Lai. [Online]. Available: http://www.sciencedirect.com/science/article/pii/S1996681416301912

[32] H. Wheeler, "Simple inductance formulas for radio coils," *Proceedings of the Institute of Radio Engineers*, vol. 16, no. 10, pp. 1398–1400, 1928.

[33] D. Kleppner and R. Kolenkow, *An Introduction to Mechanics*, 2nd ed. Cambridge University Press, 2014.

[34] E. Süli and D. Mayers, "An introduction to numerical analysis," *Cambridge University Press*, p. 328, 2003.